International Journal of Peptide Research and Therapeutics (2024) 30:3
https://doi.org/10.1007/s10989-023-10583-6

Design and Self Assembly of Tri-Terpene Peptide Conjugates and Their Interactions with EGFR and EGFR Mutant Receptors: An In Silico and In Vitro Study

Mia I. Rico[1] · Beatriz G. Goncalves[1] · Hannah L. Hunt[1] · Ipsita A. Banerjee[1]

Accepted: 29 November 2023 / Published online: 14 December 2023

Abstract

In this work, we designed new terpenoid-peptide conjugates to target the epidermal growth factor receptor (EGFR) and its double mutant EGFR T790M/L858R which are implicated in many cancers. The peptides utilized were MEGPSKCCFSLALSH (MFSL), a new peptide sequence designed by mutating an ErbB2 targeting peptide, while the sequence VPWXE was derived from a peptide motif known to target tumor cells. Each of the peptides were conjugated to four terpenoids, 23-hydroxy betulinic acid (HB), oleanolic acid, perillic acid, and ursolic acid. Molecular docking and molecular dynamics (MD) simulations with the kinase domain of both the wild type and double mutant EGFR receptors revealed that the conjugates formed H-bonds and hydrophobic interactions with key residues in the hinge region, A-loop, and DFG motif, while in the case of the double mutant, interactions also occurred with C-terminal residues and with allosteric sites. MMGBSA analysis revealed higher binding energies for the double mutant. Six of the conjugates were synthesized and self-assembled into nanoassemblies and their impact on tumor cells expressing the wild type and double mutant receptor revealed that higher apoptosis was induced by MFSL conjugates, particularly in cells expressing the double mutant EGFR receptor. The HB and ursolate conjugates were found to be more potent against the tumor cell lines. Overall, these results indicate that these peptides and peptide conjugates can effectively bind to both the wild type and the T790M/L858R receptors to target tumor cells. Such peptide conjugates may be further potentially developed as therapeutic agents for further laboratory studies against tumors overexpressing EGFR.

Keywords Molecular dynamics · Epidermal growth factor receptor (EGFR) double mutant · Peptide assemblies · Targeting

Introduction

In recent years, new strategies for cancer treatment have been developed to supplement traditional treatment methods such as chemotherapy, surgery and radiation (Debala et al. 2021). Specifically, targeted drug delivery has garnered tremendous attention due to its potential ability to mitigate side-effects caused by systemic drugs, which affect somatic cells in addition to tumor cells (Kutova et al. 2019). In receptor targeted drug delivery, specific overexpressed receptors in tumor cells are identified for targeting using designed drug molecules or ligands (Chen et al. 2010). In order to decipher receptor-ligand interactions, molecular docking studies provide critical information regarding the binding interactions (Morency et al. 2018). In silico studies allow for an extensive examination of possible drug interactions, while saving costs and valuable resources (Azuaje 2017) before synthesizing and exploring the most optimal candidate. In addition to molecular docking, molecular dynamics simulations have become key to drug discovery, as these provide in-depth analysis of receptor-ligand interactions (Durrant and McCammon 2011).

For example, docking studies were conducted with genistein, a phytoestrogen, to examine the interactions with Hypoxia Inducible Factor-1 (HIF-1α), an overexpressed protein in breast cancer, which revealed the sites of interactions and thereby provided insights into downregulation mechanisms of HIF-1α by genistein (Mukund et al. 2019). While several receptors are over-expressed in tumor cells

---

Mia I. Rico and Beatriz G. Goncalves are co-first authors.

✉ Ipsita A. Banerjee
banerjee@fordham.edu

[1] Department of Chemistry, Fordham University, 441 East Fordham Road, Bronx, NY 10458, USA

that are implicated in tumor progression and metastasis such as G-protein coupled receptors (Li et al. 2005), somatostatin receptor (Volante et al. 2008) and gonadotropin releasing hormone receptors (GnRH) (Limonta et al. 2012), growth factor receptors have particularly gained importance over the years due to the downstream signaling pathways which these receptors are associated with, that can lead to over-activation and proliferation of tumor cells (Minashi et al. 2021). These include the vascular endothelial growth factor receptor (VEGFR) (Shibuya 2011), epidermal growth factor receptor (EGFR) (Rimawi et al. 2010), platelet derived growth factor receptor (PDGFR-alpha) (Carvalho et al. 2005), and fibroblast derived growth factor receptors (FGFRs).

In addition, nanoscale materials are being developed for both active and passive targeting of tumor cells (Cheng et al. 2021) due to their tunability and multifunctional properties (Jagtap et al. 2020). Specifically, peptide-based nanomaterials are gaining popularity due to their biological recognition properties, targeting ability, and reduced toxicity toward non-cancerous cells (Costa et al. 2019). For example, a polyethylene glycol (PEG) functionalized peptide analog (X4-2-6), derived from the transmembrane helix of the chemokine receptor CXCR4, was self-assembled into nanoparticles and was found to inhibit CXCR4 function in vitro and impair CXCR4-related metastasis of MDA-MB-231 breast cancer cells (Tarasov et al. 2011). In another study, a 26-amino acid aptamer-like peptide, which was identified from phage display library to have a high binding affinity toward the fibronectin extra domain B, was conjugated with polyethylene glycol-poly lactic acid nanoparticles and encapsulated with the chemotherapeutic drug Paclitaxel to specifically target glioma cells that overexpress the protein fibronectin extra domain B. The results showed enhanced antiangiogenic activity in the tumor neovasculature and cellular internalization and apoptosis of glioma cells (Gu et al. 2014). In a separate study, lipoprotein-like core–shell nanoparticles of the tyrosine kinase inhibitor drug lapatinib were prepared with the protein bovine serum albumin (BSA) that were found to reduce proliferation of U87 glioma cells and induce apoptosis (Gao et al. 2014).

EGFR, which is overexpressed in numerous cancers, is a member of the superfamily of transmembrane tyrosine kinases (RTKs) (Maennling et al. 2019; Zhang et al. 2006; Lee et al. 2015). Specifically, the kinase domain of EGFR and other RTKs is an attractive target for developing drugs for targeting tumor cells (Purba et al. 2017; Masuda et al. 2012). Numerous drugs have been developed which target the ATP binding pocket of the receptor. For example, drugs such as erlotinib and gefitinib were considered first generation drugs that bound to the kinase domain of EGFR efficaciously (Cataldo et al. 2011) and showed excellent therapeutic response. However, those drugs were found to develop resistance over time to mutations within the receptor, such as the T790M gatekeeper EGFR mutation (Yu et al. 2014) as well as double and triple mutations such as T790M/L858R and T790M/L858R/C797S (Nguyen et al. 2009). These mutations often increase the binding affinity of kinase for ATP and thereby reduce inhibitor activity. Thus, next generation drugs were developed to overcome drug resistance to these mutations, including drugs such as Osimertinib (Zhang et al. 2016), Afatinib, Dacomitinib, and Rociletinib (Roskoski 2016, Du and Lovly 2018). However, over time, many of those drugs were also found to acquire resistance. Thus, there exists a need for development of new therapeutics that can potentially target not only the wild type over-expressed EGFR receptor, but also its mutants.

In this work, we have developed self-assembled nanoscale peptide conjugates of the triterpenoids hydroxybetulinic acid (HB), ursolic acid (UA), and oleanolic acid (OA) and examined the interactions of the conjugates with the double mutant T790M/L858R and the wild type EGFR. These naturally derived triterpenoids were selected due to their inherent anticancer activity (Yin et al. 2017; Lu et al. 2019; Tang et al. 2022). Furthermore, UA has been shown to induce apoptosis and suppress gene expression of CT45A2 in EGFR T790M tumor cells as well as reduce EGFR expression in HT-29 colon cancer cells (Shan et al. 2009). Additionally, betulinic acid and OA also downregulated EGFR activity in bladder cancer cells and melanoma cells respectively (Chadalapaka et al. 2010; Ghosh et al. 2014). We also created peptide conjugates of the menthane monoterpenoid and human metabolite, perillic acid, due to its documented antineoplastic properties (Yeruva et al. 2007). Furthermore, these compounds are derived from plants and are generally non-toxic toward somatic cells as well as hydrophobic in character, which may aid in binding to the hydrophobic binding pocket of EGFR receptors (Zhao et al. 2020). We utilized two peptides for conjugation with the terpenoids, which included the short peptide VPWXE (where X = norleucine) and the peptide sequence MEGPSKCCFSLALSH (abbreviated as MFSL). Specifically, VPWXE is derived from the p160 sequence (VPWMEPAYQRFL) which is known for its affinity toward neuroblastoma cells (Askoxylakis et al. 2006). Additionally, the VPWXE motif was incorporated into several peptide sequences that were previously designed for screening several tumor cell binding peptides using peptide array-whole cell binding technique and were shown to bind to tumor cell surface receptors (Ahmed and Kaur 2017).

The MEGPSKCCFSLALSH peptide, on the other hand, was designed by creating a mutation in the sequence MEGPSKCCYSLALSH. Through phage display library, this sequence has been shown to have a high affinity toward receptor ErbB2 (Ahmadpour and Hosseinimehr 2019), a tyrosine kinase receptor that shows 95% homology with EGFR in the intracellular region containing residues

727–986, which encompasses the EGFR kinase domain (Wang et al. 2011). To examine if binding interactions with EGFR can be enhanced, we created point mutations in the sequence to design three peptides and examined their anticancer potential using the antiCP webserver, (Vijayakumar and Lakshmi 2015). Based on the scores obtained, we selected the MEGPSKCCFSLALSH peptide sequence (abbreviated as MFSL) where the tyrosine residue in the original peptide was mutated to phenylalanine at position nine for designing the conjugates.

Thus, eight conjugates were designed with four conjugates for each sequence. The structures of the peptides and the conjugates are shown in Fig. 1. Docking studies revealed that, compared to the neat peptides, the conjugates showed enhanced binding affinities toward both the wild type and double mutant EGFR. Additionally, several

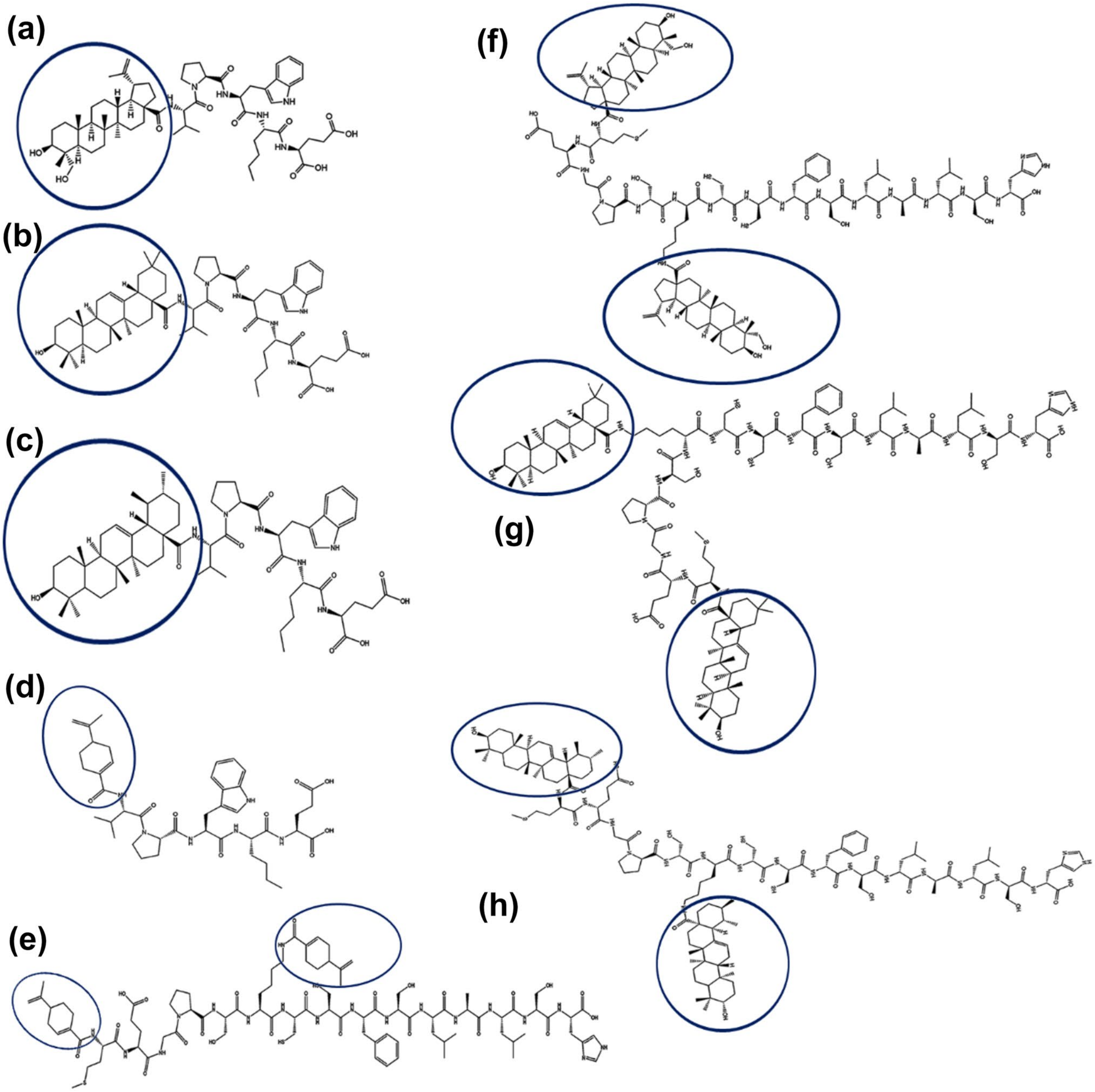

Fig. 1 Chemical structures of terpenoid-peptide conjugates designed. **a** Hydroxybetulinate-VPWXE (HB-VPWXE); **b** Oleanolate-VPWXE; **c** ursolate-VPWXE; **d** perillate-VPWXE; **e** (perillate)$_2$-MEGPSKCCFSLALSH (perillate)$_2$-MFSL); **f** (hydroxybetulinate)$_2$-MEGPSKCCFSLALSH (HB)$_2$-MFSL); **g** oleanolate-MEGPSKCCFSLALSH (oleanoate)$_2$-MFSL); **h** (ursolate)$_2$- MEGPSKCCFSLALSH (ursolate)$_2$-MFSL). In each case, the terpene moiety has been circled

of the conjugates were able to bind to the DFG motif residue D831 of the activation loop in the wild type receptor, while binding occurred both with C-terminal residues and binding pocket residues for the double mutant. To validate the computational results, six of the optimum conjugates were synthesized and self-assembled into nanoassemblies to target tumor cells expressing the wild type (WT) EGFR and T790M/L858R receptor. While monoconjugates were designed with VPWXE peptide, di-conjugates were designed for the MFSL peptide, because of the presence of two free amines in the MFSL sequence. Depending upon the conjugates, multilayered supramolecular assemblies or nanofibers and nanospheres were formed. In vitro studies revealed that the MFSL-tri-terpenoid conjugates induced higher apoptosis in the wild type EGFR expressing cells and the double mutant, while the VPWXE conjugates with ursolate and hydroxybetulinate also induced apoptosis in the T790M/L858R expressing cells. In contrast, most of the conjugates had comparatively little effects on non-cancer cells. Thus, we have designed new triperpene-peptide conjugates with applications for specifically targeting over-expressed EGFR receptors and the T790M/L858R receptor. Specifically, the ursolate and the hydroxybetulinate conjugates may be potentially developed for future in vivo studies for therapeutic applications.

Materials

The peptides, MEGPSKCCFSLALSH (MFSL) and VPW(Nle)E (VPWXE), were custom ordered from GenScript. Oleanolic acid, 23-Hydroxybetulinic acid, and ursolic acid were purchased from SantaCruz Biotechnology. Dimethylformamide (DMF), Dimethyl sulfoxide (DMSO), *N*-hydroxysuccinimide (NHS), 1-ethyl-3-(3-dimethylaminopropyl) carbodiimide (EDAC) and Poly (Glu, Tyr) sodium salt were purchased from Sigma-Aldrich. Mouse fibroblast cells (SCRC-1008), F98$_{\text{EGFR}}$ (ATCC CRL-2948) rat glioma cells with wild type over-expressed EGFR and human NCI-H1975 lung cancer cells (CRL-5908) expressing EGFR [T790M/L858R] were purchased from ATCC (Manassas, VA, USA) along with fetal bovine serum (FBS), Dulbecco's modified Eagle's medium (DMEM), Dulbecco's phosphate-buffered saline (PBS), Antibiotic–Antimycotic, and Penicillin–Streptomycin-Amphotericin B Solution. The MTT Assay Kit and the Annexin V FITC-Propidium Iodide Assay Kit were purchased from Cayman Chemical Company (Ann Arbor, MI, USA). The Kinase-Glo Luminescent Assay was purchased from Promega (Madison, WI). EGFR and EGFR (T790M/L858R) proteins were purchased from Thermo Fisher Scientific.

Computational Methods

Prediction of Anticancer Potential of Peptides

We investigated the anti-cancer properties of the peptides VPWXE, as well as MEGPSKCCYSLALSH and its mutants. In the case of MEGPSKCCYSLALSH, point mutations were generated at three positions, namely positions 2, 9 and 11 by replacing E with D at position 2; Y with F at position 9 and L with I at position 11. The anti-cancer potential of those peptides was studied through the web server AntiCP (https://webs.iiitd.edu.in/raghava/anticp/submission.php). The program determines various physiochemical properties of each peptide including hydrophobicity, hydropathicity, hydrophilicity, and pI, and provides a support vector machine (SVM) score, which is determined by amino acid composition, dipeptide composition, and binary profile pattern. The two peptides with the highest SVM score were used for designing the conjugates. Those peptides were MEGPSKCCFSLALSH (abbreviated as MFSL) and VPW(Nle)E (VPWXE).

Peptide Design

We utilized ChemDraw (20.1.1) to design each conjugate, peptide and the neat terpenes followed by ChemDraw 3D (20.1.1) where each structure was energy minimized to relieve any structural strain. The files were then exported as a .pdb file and utilized for further studies.

Receptor Processing

For this analysis, .pdb files of wild type EGFR kinase domain (PDB ID: 2GS2) (Lelais et al. 2016) and EGFR T790M/L858R kinase domain (PDB ID: 3W2R) (Worm et al. 2020) were downloaded from the online RCSB Protein Data Bank as .pdb files. Each file was then opened on PyMOL (2.5.2). Water molecules and any bound ligands where applicable were removed. The final structures were then exported as a .pdb file to be used for further studies.

Surface Cavity Analysis

The web server Pocket-Cavity Search Application (POCASA) was used to determine the surface cavities and binding pockets of the receptors. This server predicts ligand binding sites by rolling a sphere probe of different radii along the protein surface to detect pockets, ranking these by position and size (Yu et al. 2010). For our studies, a probe radius of 2 Å, a single point flag of 16, a protein depth flag of 18, and a grid size of 1 Å was used. We then exported the results into PyMOL to visualize the cavities.

Docking Studies

Molecular docking studies were conducted for both receptors with each of the conjugates, peptides VPWXE and MEGPSKCCYSLALSH, as well as neat ursolic acid, perillic acid, oleanolic acid and 23-hydroxy betulinic acid (HB) using the molecular docking software AutoDock Vina 1.1.2, which uses gradient optimization and multithreading, thus speeding up and improving accuracy of the molecular docking (Trott and Olson 2012). We prepared the receptor-ligand complexes using AutoDock Tools 1.5.6. The receptor was first prepared by opening it on the workspace of AutoDock Tools 1.5.6 where polar hydrogens were added along with Kollman charges. The file was then saved as a .pdbqt file. On a different workspace window, the ligand that had been prepared on ChemDraw3D was saved as a.pdbqt file. Both the .pdbqt receptor and ligand files were then opened on the same workspace where an automatic grid box (40 × 40 × 40) Å with specific coordinates for each receptor was created. We recorded the highest binding affinities of each docked receptor-ligand and visualized the results using PyMOL.

Receptor-Ligand Interactions (PLIP)

Each receptor-ligand complex structures with the highest binding affinity were exported into the Protein–Ligand Interaction Profiler (PLIP). PLIP is a web server (https://plip-tool.biotec.tu-dresden.de/plip-web/plip/index) which can analyze .pdb files generated from docking studies by identifying hydrogen bonds, hydrophobic interactions, and their interacting residues (Salentin et al. 2014). The interaction results were recorded and PyMOL was used for further visualization and analysis.

Molecular Dynamics

To conduct molecular dynamics simulations, the software Desmond was utilized. This software is used to study biological systems at high-speeds with high performance and accuracy, using specific advanced algorithms and numerical techniques (Bowers et al. 2006; Bergdorf et al. 2016). We chose each receptor-ligand complex with the highest binding affinity from the AutoDock runs, added hydrogens, and uploaded it to the software Maestro. We then ran Protein Preparation Wizard on each receptor by assigning bond orders, adding hydrogens, creating zero-order bonds to metals, and generating het states using Epik with a pH of 7.0 ± 2.0. After the receptor was preprocessed with these conditions, we optimized it using a PROPKA pH of 7.0. We then incorporated the ligand with the prepared receptor and created a solvated system using System Builder. We predefined the solvent model with SPC, used an orthorhombic box shape with distances of 10 Å on all sides, and minimized the volume of the box to best fit the complex. The system was neutralized by adding Na^+ and Cl^- ions. All systems were run locally on Maestro 2020-4. We then ran the simulations using force field OPLS2005 (Banks et al. 2005) with a 100 ns trajectory, an NPT ensemble class, and conditions set at 300 K and 1.013 atm pressure. This process was conducted for each receptor-ligand combination. The results of each complex were then analyzed. The radius of gyration, molecular surface area, and RMSD data were obtained using the plot function on Maestro.

MMGBSA Studies

Molecular mechanics generalized Born surface area (MM-GBSA) calculations were carried out to determine the theoretical free energies of binding of each peptide and the conjugates with each receptor (Genheden and Ryde 2015). The MM-GBSA method calculates free energies of binding complexes by using molecular mechanics calculations and solvation models (Forouzesh and Mishra 2021). The free energy of binding, $\Delta G_{(bind)}$, can be calculated using the equation $\Delta G_{(bind)} = \Delta G_{(solv)} + \Delta E_{(MM)} + \Delta G_{(SA)}$. The ΔG_{solv} is the difference in solvation energy of the ligand-bound receptor complex and the sum of the solvation energies for the free ligand and receptor. ΔE_{MM} is the difference in the minimized energies between the receptor-ligand complex and the sum of the energies of each of the free ligands and receptor, while $\Delta G_{(SA)}$ is the difference in surface area energies of the ligand-receptor complex and the sum of the surface area energies for each of the neat ligands and receptors (Dasmahapatra et al. 2022). To assess the polar effect of free energy, a generalized Born model was used with an external dielectric constant of 80 and an internal dielectric constant of 1. The non-polar energy contribution is calculated from the solvent accessible surface area (SASA). The prime MM-GBSA module of the Schrodinger suite was used to calculate the free energies, which calculates the energy of optimized free receptor, free ligand, and ligand bound with receptor (Kumar et al. 2022). The ligand strain energy is also calculated by placing the ligand in a solution which was auto generated by VSGB 2.0 suit.

Laboratory Methods

Synthesis

To validate the computational results, we synthesized six of the optimal conjugates and tested them in vitro. Thus, peptide conjugates of hydroxybetulinic acid (HB), oleanolic acid, and ursolic acid were prepared with VPWXE and MEGPSKCCFSLALSH (MFSL). In the case of MFSL, di-conjugates were prepared, where the free amino groups of lysine and methionine residues were conjugated with the triterpene. Monoconjugates of VPWXE were prepared where the N-terminal of valine was conjugated with the triterpenes. For the synthesis of conjugates, traditional peptide coupling methods were used (Fischer 2010). Briefly, each triterpenoid (0.053 M) was dissolved separately in dimethyl formamide (DMF) followed by the addition of *N*-hydroxy-succinimide (NHS) (0.06 M) and 1-ethyl-3-(-3-dimethylaminopropyl) carbodiimide hydrochloride (EDAC) (0.08 M) to activate their carboxylic groups. In the case of the MFSL conjugates, 0.1 M concentrations of the triterpenes were used. Each of these were then shaken at 200 rpm for an hour at 4 °C. Next, the respective peptide (0.1 M) was added, and allowed to shake for 24–48 h at 4 °C. The solvent was then evaporated via rotary evaporation. The products obtained were then recrystallized from acetone or methanol. The residual solvent was removed and dried by using a speed-vacuum concentrator. The chemical structures of the conjugates were confirmed by proton NMR spectroscopy conducted using a Bruker 400 MHz NMR in DMSO-d6 with 0.3% TMS.

Ursolate-VPWXE: δ 0.69 (3H, s); δ 0.85 (18H, m); δ 0.94 (7H, m); δ 1.08 (6H, m); 1.25 (2H, m); δ 1.32 (6H, t); δ 1.41 (1H, m); δ 1.46 (1H, m); δ 1.58 (2H, t); δ 1.61 (6H, m); δ 1.81 (4H, m); δ 2.01 (4H, m); δ 2.22 (5H, m); δ 2.38 (4H, t); δ 3.11 (2H, d); δ 3.41 (1H, t); δ 3.52 (2H, t); δ 4.32 (1H, d); δ 4.40 (1H, t); δ 4.50 (1H, s); δ 4.64 (1H, t); δ 4.92 (1H, s); δ 5.12 (1H, t); δ 5.25 (1H, s); δ 6.8 (1H, d); δ 7.1 (1H, d); δ 7.4 (1H, d); δ 7.7 (1H, d); δ 8.5 (4H, s); δ 10.30 (1H, s); δ 12.25 (2H, s).

Oleanolate-VPWXE: δ 0.72 (6H, s); δ 0.83 (3H, s); δ 0.92 (12H, m); δ 1.00 (7H, m); δ 1.15 (6H, m); δ 1.22 (2H, m); δ 1.38 (6H, m); δ 1.43 (4H, m); δ 1.52 (2H, t); δ 1.68 (2H, q); δ 1.81 (4H, m); δ 1.94 (4H, m); δ 2.12 (2H, t); δ 2.19 (2H, d); δ 2.35 (7H, m); δ 3.15 (2H, d); δ 3.42 (1H, t); δ 3.58 (2H, t); δ 4.25 (1H, d); δ 4.49 (2H, m); δ 4.62 (1H, t); δ 4.82 (1H, s); δ 4.95 (1H, t); δ 5.20 (1H, s); δ 7.22 (1H, s); δ 7.63 (d, 1H); δ 6.81 (d, 1H); δ 7.2 (d, 1H); δ 7.6 (1H, d); δ 8.33 (4H, s); δ 10.25 (1H, s); δ 12.51 (2H, s).

Hydroxybetulinate-VPWXE δ 0.65 (3H, s); δ 0.76 (3H, s); δ 0.82 (15H, m); δ 0.95 (7H, m); δ 1.1 (1H, t); δ 1.20 (2H, m); δ 1.30 (5H, m); δ 1.45 (1H, s); δ 1.54 (6H, m); δ 1.72 (8H, m); δ 1.81 (3H, s); δ 2.1 (1H, t); δ 2.2 (4H, m); δ 2.40 (4H, t); δ 2.96 (2H, d); δ 3.20 (1H, t); δ 3.42 (2H, t); δ 3.82 (1H, s); δ 4.30 (1H, d); δ 4.40 (1H, s); δ 4.52 (1H, t); δ 4.61 (1H, t); δ 4.82 (1H, s); δ 4.90 (2H, m); δ 5.30 (1H, s); δ 6.5 (1H, s); δ 7.0 (2H, m); δ 7.5 (1H, d); δ 7.8 (1H, d); Δ 8.51 (4H, s); δ 10.20 (1H, s); δ 12.50 (2H, s).

(Ursolate)$_2$-MEGPSKCCFSLALSH: δ 0. 80 (6H, d); δ 0.87 (30H, s); δ 0.96 (2H, t); δ 1.0 (12H, s); δ 1.1 (12H, d); δ 1.21 (2H, t); δ 1.32 (4H, t); δ 1.40 (4H, t); δ 1.44 (4H, d); δ 1.51 (5H, m); δ 1.60 (14H, m); δ 1.65 (4H, m); δ 1.75 (10H, m); δ 1.85 (4H, t); δ 2.0 (9H, m); δ 2.22 (4H,d); δ 2.31 (6H, m); δ 2.7 (2H, t); δ 2.95 (6H, d); δ 3.0 (4H, m); δ 3.25 (2H, t); δ 3.4 (2H, t); δ 3.9 (2H, s); δ 4.11 (6H, d); δ 4.35 (5H, t); δ 4.50 (3H, t); δ 4.60 (1H, q); δ 4.70 (2H, t); δ 4.75 (2H, s); δ 4.80 (2H, t); δ 4.85 (1H, t); δ 5.0 (3H, s); δ 5.1 (1H, t); δ 7.0 (4H, d); δ 7.25 (1H, d); δ 7.8 (1H, s); δ 8.25 (15H, s); δ 8.60 (1H, s); δ 9.20 (1H, s); δ 12.5 (1H, s); δ 12.82 (2H, s).

(Oleanolate)$_2$-MEGPSKCCFSLALSH: δ 0.80 (6H, s); δ 0.85 (12H, s); δ 0.95 (26H, m); δ 1.0 (6H, s); δ 1.1 (2H, d); δ 1.22 (2H, m); δ 1.30 (8H, m); δ 1.45 (7H, d); δ 1.50 (6H, m); δ 1.65 (10H, m); δ 1.70 (4H, q); δ 1.80 (4H, q); δ 1.85 (6H, m); δ 1.95 (4H, t); δ 2.10 (9H, m); δ 2.25 (4H, d); δ 2.30 (6H, t); δ 2.6 (2H, t); δ 3.0 (2H, d); δ 3.15 (6H, m); δ 3.35 (2H, t); δ 3.42 (2H, d); δ 3.55 (2H, t); δ 4.0 (2H, s); δ 4.15 (6H, d); δ 4.35 (5H, t); δ 4.50 (3H, t); δ 4.62 (2H, m); δ 4.70 (1H, s); δ 4.85 (2H, t); δ 4.90 (1H, t); δ 5.10 (3H, s); δ 5.3 (2H, t); δ 7.2 (4H, s); δ 7.3 (1H, d); δ 7.5 (1H, s); δ 8.2 (14H, s); δ 8.3 (1H, s); δ 8.9 (1H, s); δ 11.9 (1H, s); δ 13.1 (2H, s).

(Hydroxybetulinate)$_2$-MFSL: δ 0.75 (6H,s); 0.82 (18H, m); δ 1.0 (12H, d); δ 1.05 (6H, m); δ 1.25 (2H, m); δ 1.40 (7H, m); δ 1.55 (18H, m); δ 1.65 (16H, m); δ 1.70 (4H, t); δ 1.82 (12H, m); δ 1.90 (4H, t); δ 2.0 (2H, m); δ 2.1 (9H, m); δ 2.35 (4H, t); δ 2.50 (2H, t); δ 2.80 (2H, d); δ 3.20 (6H, m); δ 3.30 (2H, t); δ 3.40 (2H, d); δ 3.5 (6H, m); δ 3.9 (2H, s); δ 4.20 (6H, d); δ 4.35 (5H, t); δ 4.5 (3H, t); δ 4.6 (1H, q); δ 4.70 (1H, t); δ 4.80 (1H, s); δ 4.85 (2H, t); δ 4.95 (3H, m); δ 5.1 (3H, s); δ 5.3 (2H, d); δ 7.2 (4H, s); δ 7.3 (1H, d); δ 7.5 (1H,s); δ 8.0 (1H, s); δ 8.1 (14H, s); δ 8.8 (1H, s); δ 12.1 (1H, s); 12.6 (1H, s); δ 12.9 (1H, s).

Self-Assembly

The products, (0.2 M) were then each allowed to self-assemble in aqueous conditions containing 2% DMF at room temperature over a period of 2 to 3 weeks. Over time, the formation of the nanoassemblies was monitored using Dynamic Light Scattering (DLS). The formed assemblies were then centrifuged, washed with water thrice, and dried before further analysis.

Dynamic Light Scattering (DLS)

To assess the formation of the assemblies in suspension over time, Dynamic Light Scattering (DLS) studies were conducted using a Zetasizer Ultra from Malvern Panalytical. Having confirmed the formation of nanoassemblies, these samples were then used for further studies.

Atomic Force Microscopy (AFM)

Atomic Force Microscopy was utilized to assess the morphology of the formed nanoassemblies. Each sample was spread on a mica sheet and allowed to air-dry for 24 h prior to analysis. Images were then captured at multiple locations using contact mode or ScanAsyst mode on a Bruker multimode 8 atomic force microscope. A CONTV cantilever was used with frequency of 13 kHz, spring constant of 0.2 N/m, and tip radius of 10 nm for contact mode, while a SCANASYST-AIR cantilever with frequency 70 kHz with spring constant of 0.4 N/m and tip radius of 650 nm was used while imaging using ScanAsyst mode.

Scanning Electron Microscopy (SEM)

SEM imaging was carried out using a Zeiss EVO MA10 model scanning electron microscope. Samples were dried onto conductive carbon adhesive tabs (Electron Microscopy Sciences) and were examined at a range of 8 to 15 kV at varying magnifications. The instrument was operated in EP mode.

Nanoparticle Tracking Analysis (NTA)

To examine the aggregation behavior, hydrodynamic particle sizes and concentration of the nanoassemblies, NTA analysis was carried out using a ZetaView Nanoparticle Tracking Analysis (NTA) instrument equipped with a sample chamber with a 488 nm laser. Zetaview software (Particle Metrix) was used to analyze the data obtained. In general, all samples were diluted in phosphate buffer saline (PBS) at pH 7 and studies were carried out at 25 °C. Samples were injected into the sample chamber until the liquid reached the tip of the nozzle. Each sample was run thrice and data shown are the mean values obtained from three runs.

Cell Studies

Three different cell lines were used to investigate the interactions of the nanoassemblies with each cell line. Mouse fibroblast cells (SCRC-1008) were used as the control non-cancerous cell line. For the cancer-cell lines, $F98_{EGFR}$ (ATCC CRL-2948) rat glioma cells that express wild type EGFR and human NCI-H1975 lung cancer cells (CRL-5908) expressing EGFR [T790M, L858R] were used. Each cell line was cultured in DMEM supplemented with 10% fetal bovine serum (FBS), antibiotic–antimycotic mixture (20 µg/mL) and penicillin/streptomycin (100 µg/mL). These were then incubated at 37 °C and 5% CO_2 where cells were grown to confluence. The media was replaced every 2–3 days and the cells were split twice a week.

Cell Viability and Morphology Studies

To examine cell viability, a 3-(4,5-dimethylthiazolyl-2)-2, 5-diphenyltetrazolium bromide (MTT) assay was conducted (Ghasemi et al. 2021). The cells expressing EGFR and EGFR [T790M/ L858R] were plated at a density of 1×10^5 cells/well on a 96-well Falcon polystyrene plate and incubated for 3 h at 37 °C in a 5% CO_2 incubator to allow for the cells to attach and spread in the well plates. Cells were plated in triplicate. The nanoassemblies, terpenes or peptides were then added to the cells and allowed to incubate with the cells for 24 h. For preparing nanoassemblies for cell studies, the samples were first dried in speedvac concentrator for 48 h, and then dispersed in DI water at the appropriate concentration. Dose dependent curves were obtained to determine cytotoxicity of the conjugates at a range of concentrations between 0.1 µM and 40 µM. IC-50 values were obtained using linear regression analysis using the GraphPad 9.5.0 software. Prior to the MTT assay, the cells were imaged with an inverted Amscope IN480TC-20MB13 microscope at different magnification levels to examine the morphology of the cells after exposure to the nanoassemblies. After 24 h of incubation, 10 µL of MTT reagent was added to each well, followed by an incubation period of 3 h at 37 °C. Next, 100 µL of crystal dissolving solution was added followed by 8 h of incubation at 37 °C. The absorbance at 590 nm was read immediately after, using a BioTek Eon microplate reader. The background control (MTT solution with media in the absence of cells) was subtracted from all readings. The absorbance values were then averaged for each construct treated cells as well as the control untreated cells. The viability was obtained by dividing the values obtained for the treated cells by control untreated cells and then multiplying by 100 to determine percentages. Each of these were carried out in triplicate and statistical analysis was carried out using Student's t tests to determine p values.

Apoptosis Assay

A BD FACSMelody flow cytometer was used for apoptosis studies. Flow cytometry uses different fluorochromes with varying emission and excitation to distinguish between different populations of cells (McKinnon 2018). The apoptosis assay was conducted using Annexin V FITC-Propidium Iodide (Rieger et al. 2011). The cells were plated at a density of 1×10^6 cells/well on a 6-well Falcon polystyrene plate. The nanoassemblies (3 µM) were incubated for 24 h at 37 °C with the cells. After trypsinization, the cells were then centrifuged at 400 g for five minutes. The pellet was then resuspended in 1X Binding Buffer followed by another round of centrifugation. The supernatant was decanted and the pellet was resuspended in 50 µL of Annexin V FITC/Propidium Iodide staining solution and incubated in the dark at room temperature for 10 min. Then 150 µL of 1X Binding Buffer was added along with FACS buffer (50 mL of 1 × PBS, 1% bovine serum albumin, and 0.05% sodium azide). The contents of the centrifuge tube were then passed through filter caps into FACS test tubes and loaded into the instrument for flow cytometry. Each sample was read at an excitation of 488 nm and emission of 525 nm for the Annexin V FITC staining solution and 655–730 emission for the propidium iodide (PI) staining solution. The total number of events was kept at 10,000 for every sample. Result analysis was then carried out on the software FlowJo v10.8. Each scatter plot was gated on the FSC-A/SSC-A control pseudo color plot, followed by the FSC-A/FSC-W and SSC-A/SSC-W plots. The population was then plotted as Annexin FITC- A/Propidium Iodide-A with a biexponential scale to incorporate all events in each window of the quadrant gate. The gates were then all copied to the remaining samples to quantify the frequency of each event.

Kinase Glo Assay

To confirm whether the nanoassemblies affected kinase activity of the EGFR receptors (both wild type and the double mutant), a Kinase-Glo Luminescent Assay was conducted (Bell and Storey 2014). This assay indicates the amount of ATP remaining in solution following a kinase reaction, which is quantified through luminescence measurement, where higher luminescence indicates better kinase inhibition as the remaining ATP cannot be dephosphorylated. First, various optimizations were conducted. The first consisted of optimizing the kinase reaction conditions with respect to the amount of kinase and kinase substrate. To determine the optimal substrate concentration, twofold serial dilutions (0.25–4 μg/mL) of the kinase substrate, Poly (Glu, Tyr) sodium salt, was conducted with 10 μg/mL kinase and 80 μM ATP. The plate was then incubated for an hour at room temperature to allow the kinase reaction to occur. Following the incubation period, Kinase-Glo Reagent was added to each well to double the total volume. The plate was once again incubated for 10 min in the dark at room temperature, after which its luminescence was recorded using a Biotek Eon Synergy H1 Multi-Mode Microplate Reader at an integration time of 0.25 s and at a gain of 145. The optimal kinase substrate concentration was determined to be 0.25 μg/mL, which was the concentration at which the largest change in luminescence was seen when comparing the kinase reaction wells to those that did not contain kinase. Next, we determined the optimal kinase concentration. For this, a series of twofold serial dilutions of kinase (0.625–10 μg/mL) was created along with the previously determined optimum substrate concentration and 80 μM of ATP. The same procedure was then used to arrive at a kinase optimum concentration.

Once the optimum concentration of substrate and kinase had been determined, the nanoassemblies were screened. To each well, 5 μL of 3 μM nanoassemblies in aqueous solution containing 2% DMSO was added followed by 15 μL of 2.5X the optimal concentration of WT EGFR or EGFR (T790M/L858R) kinase and Poly (Glu, Tyr) sodium salt (0.625 μg/mL) diluted in 1X kinase reaction buffer (40 mM Tris [pH 7.5], 20 mM $MgCl_2$ and 0.1 mg/mL BSA). The ATP concentration used was 5 μM. The plate was then incubated for an hour at room temperature to allow the kinase reaction to take place. After the incubation period, 50 μL of Kinase-Glo Reagent was added to each well, followed by incubation for another 10 min at room temperature. The control wells were prepared under the same conditions where aqueous solutions containing 2% DMSO was utilized. The luminescence was then recorded using a BioTek SynergyH1 microplate reader at an integration time of 0.5 s.

Results and Discussion

Prediction of Anticancer Properties of Peptides

To predict if the designed peptides exhibited anticancer properties, the sequences were uploaded into the AntiCP webserver. Results obtained are shown in Table 1. We first examined the original MEGPSKCCYSLALSH sequence as discussed earlier and compared it to the point mutations that were created. Each mutated residue is indicated in bold (at positions 2, 9 and 11).

As can be seen, the sequence with mutation at position 9 (MEGPSKCC**F**SLALSH) exhibited a high support vector machine (SVM) score of 0.94, which was higher than that

Table 1 Anti-cancer peptide screening

Peptide sequence	SVM score	Hydrophobicity	Hydropathicity	Hydrophilicity	pI	Anti-CP prediction
MEGPSKCCYSLALSH	0.91	– 0.08	0.00	– 0.22	7.03	Yes
M**D**GPSKCCYSLALSH	0.85	– 0.08	0.00	– 0.22	7.03	Yes
MEGPSKCC**F**SLALSH	0.94	– 0.04	0.27	– 0.23	7.03	Yes
MEGPSKCCYS**I**ALSH	0.91	– 0.06	0.05	– 0.22	7.03	Yes
VPW(Nle)E	1.10	0.04	– 0.36	– 0.38	4.00	Yes

Mutated residues are indicated in bold

of the original peptide MEGPSKCCYSLALSH known to bind to ErbB2 as described earlier. The mutation at position 2 resulting in the sequence M**D**GPSKCCYSLALSH on the other hand, displayed the lowest score with a SVM value of 0.85. Thus, all of the peptides with the exception of MDGPSKCCYSLALSH displayed a score of 0.9 (90%) or above and therefore were predicted to be anticancer peptides (Ghandehari et al. 2015). We also investigated the anticancer potential of the VPWXE peptide, and this peptide was found to have the highest SVM score at 1.10 and was also predicted to be an anticancer peptide. Furthermore, analysis of the physicochemical properties of the anticancer peptides showed that the mean hydrophobicity score was relatively higher for the VPWXE sequence compared to the other sequences, which is expected given the presence of all hydrophobic residues in the sequence with the exception of glutamic acid residue. Conversely, the mean hydrophilicity score was lowest for the VPWXE sequence, followed by MEGPSKCC**F**SLALSH. VPWXE also had a lower pI, while all others showed a pI of 7.0 indicative that those peptides were neutral. Therefore, these two peptides were utilized in further computational and experimental studies.

Cleft Determination

To determine the binding pockets of the kinase domains of the receptors, we utilized the web server POCASA. This server predicts the number of possible binding pockets, as well as their rank, volume, and their volume depth (VD). The results are shown in Fig. 2 and Table 2. As shown in Table 2, the wild type EGF receptor displayed five binding pockets and the highest ranked pocket was number 264, which was found to have a volume of 385 Å and a VD value of 1059. The number of binding pockets increased in the EGFR T790M/L858R receptor to 6 pockets. Pocket number 204 was ranked highest with a volume of 324 Å and a VD of 1264. Thus, though there was a slight decrease in the volume of the highest ranked pocket in the EGFR T790M/L858R, the volume depth value (VD) increased. This value is determined by addition of the depth of all pocket points, where the depth of each pocket point has been established to be the smallest distance from a pocket point to probe surface (Ramirez and Caballero 2018). Therefore, it is likely that the binding of the ligands would occur deeper into the receptor for the double mutant compared to the wild type.

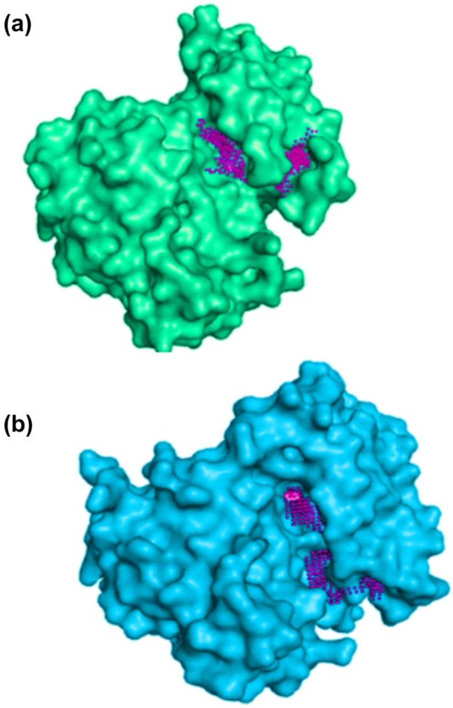

Fig. 2 POCASA results showing binding pockets of EGFR kinase domains. **a** wild type receptor; **b** T790M/L858R Double mutant receptor. Purple regions indicate binding pockets

Table 2 Binding pockets predicted by POCASA

Rank number	Pocket number	Volume (Å)	VD
Wild Type EGFR			
1	264	385	1059
2	409	256	641
3	14	169	492
4	88	159	400
5	366	96	243
EGFR T790M/L858R			
1	204	324	1264
2	75	148	373
3	400	115	295
4	488	28	72
5	208	23	58
6	422	21	46

Molecular Docking Studies and PLIP Analysis

To determine the binding affinities and interactions between each conjugate and peptide with the receptors, we conducted molecular docking studies using the software Autodock Vina 2.0. The results obtained for binding affinities are shown in Table 3. The highest binding affinity was obtained for the ursolate-VPWXE conjugate with the double mutant receptor followed by hydroxybetulinate-VPWXE (HB-VPWXE) conjugate, also for the double mutant receptor. The lowest binding affinity was seen for the (perillate)$_2$-MFSL conjugate with the wild type EGFR receptor. Interestingly, all VPWXE-conjugates showed higher binding affinities compared to the MFSL conjugates. Additionally, the neat compounds were also found to show higher binding affinities

Table 3 Binding affinities determined by Autodock Vina

	Binding affinity kcal/mol	
	EGFR (Wild Type)	EGFR T790M/L858R
HB-VPWXE	− 7.9	− 9.0
Oleanoate-VPWXE	− 8.6	− 8.2
Perillate-VPWXE	− 7.4	− 6.5
Ursolate-VPWXE	− 8.4	− 9.4
VPWXE	− 6.6	− 8.2
$(HB)_2$-MFSL	− 7.1	− 7.3
$(oleanolate)_2$-MFSL	− 6.2	− 5.5
$(perillate)_2$-MFSL	− 5.1	− 6.4
$(ursolate)_2$-MFSL	− 7.0	− 6.3
MFSL	− 5.4	− 6.5
Hydroxybetulinic acid	− 7.7	− 6.8
Oleanolic acid	− 8.4	− 8
Perillic acid	− 6.6	− 5.5
Ursolic acid	− 8.4	− 8.5

compared to the MFSL conjugates, with the exception of $(HB)_2$-MFSL and $(perillate)_2$-MFSL conjugates, which showed increased binding affinity toward the T790M/L858R double mutant receptor compared to the corresponding neat HB and perillate compounds.

To further elucidate these results, we conducted PLIP studies to determine the residues of the receptors involved in binding with the conjugates and peptides. For interactions VPWXE and its conjugates with the wild type receptor, results are shown in Supplementary Information Table S1a and in Fig. 3. The VPWXE conjugates, as well as the peptide alone, were found to bind within the binding pocket of the kinase domain (Kumar et al. 2008). As expected, a higher number of hydrophobic interactions were observed for all conjugates compared to the neat peptide due to the presence of the terpene moieties. The neat peptide, on the other hand, showed eight hydrogen bonds and only four hydrophobic interactions. Furthermore, neat VPWXE and all conjugates with the exception of ursolate-VPWXE and perillate-VPWXE were found to form H-bonds with the catalytic loop residues (either ASN 818 or ARG 817 or both). Perillate-VPWXE and ursolate-VPWXE, on the other hand, formed H-bonds with the DFG motif residue ASP 831, as did the neat peptide. The DFG motif is an important residue for designing EGFR inhibitors due to its role in regulating kinase activity and H-bonds with the ASP 831 residue in particular have shown to be beneficial in the formation of binding complexes with the wild type receptor (Peng et al. 2013). Interestingly, the highest number of hydrophobic interactions was seen for HB-VPWXE and perillate-VPWXE, both with eleven interactions. The HB-VPWXE conjugate interacted with residues from the Gly-rich P-loop region (LEU 694, ALA 698, PHE 699) and with the activation loop residues ASP 831 (DFG motif) and LEU 834. Interactions were also observed with the catalytic loop residues ARG 817 and LEU 820, which have been implicated in binding interactions of other EGFR inhibitors, including hydrophobic interactions with quinazolinone-benzyl piperidine derivatives (Emami et al. 2022). It is important to note that the terpene ring system was involved primarily in hydrophobic interactions. In addition, hydrophobic interactions were also seen with LYS 721.

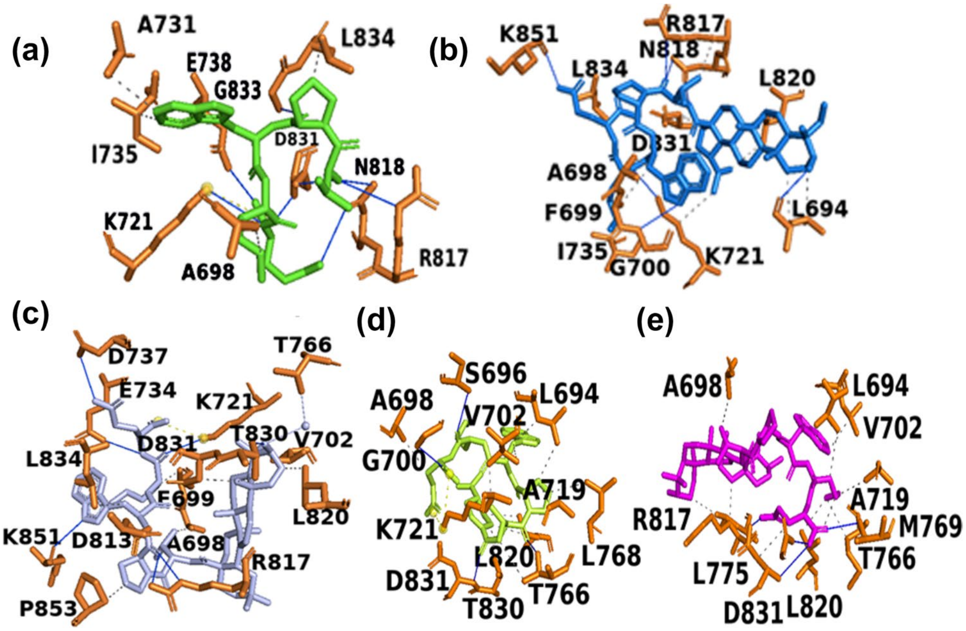

Fig. 3 Binding interaction analysis of VPWXE conjugates obtained from PLIP with wild type EGFR. **a** VPWXE; **b** HB-VPWXE; **c** oleanolate-VPWXE; **d** perillate-VPWXE and **e** ursolate-VPWXE

Oleanolate-VPWXE and ursolate-VPWXE showed hydrophobic interactions roughly in the same region. However, it is important to note that oleanolate-VPWXE, like neat VPWXE and perillate-VPWXE, was found to form a salt bridge with LYS 721. This interaction has been shown to be critical because LYS 721 usually forms a salt bridge with the highly conserved GLU 738 residue, which is important for the catalytic activity of kinase. Thus, the fact that these two conjugates and neat VPWXE form a salt bridge with LYS 721 implies that the salt bridge with GLU 738 is disrupted when these conjugates bind to the active site (Bose and Zhang 2009; Honegger et al. 1987). This is compelling as several kinase inhibitors including Erlotinib, indoline derivatives, and Midostaurin have been shown to interact with LYS 721 (Mirza et al. 2015; Palanivel et al. 2022). The perillate-VPWXE also interacted with Gly-rich-P loop residues such as SER 696, GLY 700, LEU 694, ALA 698 and VAL 702 in addition to other residues in the binding pocket such as THR 830 and LEU 820. One study found that the EGFR inhibitor, erlotinib, and several erlotinib analogues formed many similar interactions with EGFR as perillate-VPWXE, specifically with residues LEU 694, VAL 702, and THR 830, indicating that these interactions are likely important for the targeting ability of the conjugate (Sheikh and Hassan 2016).

We then compared the interactions of the double mutant T790M/L858R EGFR receptor with VPWXE and its conjugates (Fig. 4 and Supplementary Information S1b). As with the wild type receptor, the VPWXE conjugates and the peptide interacted primarily within the ATP binding pocket. However, the residues involved were markedly different. No salt bridges or interactions were seen with LYS 721. Instead, we observed a salt bridge and a H-bond with LYS 745 for VPWXE peptide. LYS 745 is considered a critical residue involved in binding to ATP and drugs such as gefitinib (Iressa) are known to bind to this site and exert inhibitory effects (Barker et al. 2001).

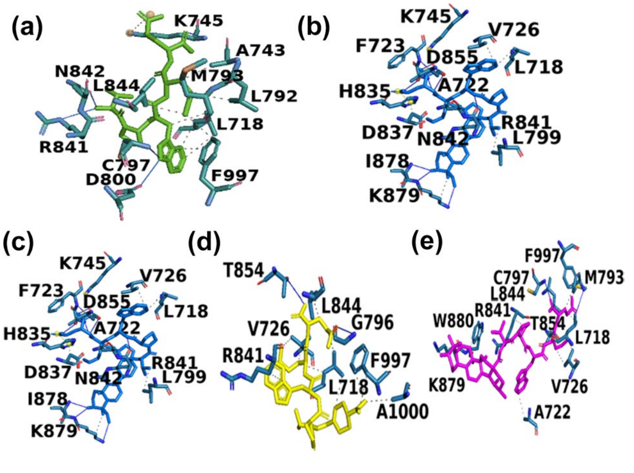

Fig. 4 Binding interaction analysis of VPWXE and its conjugates with T790M/L858R EGFR obtained from PLIP. **a** VPWXE; **b** HB-VPWXE; **c** oleanolate-VPWXE; **d** perillate-VPWXE and **e** ursolate-VPWXE

Other vital H-bonds included those with residues CYS797, ARG 841, ASN 842 and ASP 800. Furthermore, it appears that hydrophobic interactions occurred further into the C-terminal with PHE 997. Additional hydrophobic interactions included those with LEU 718, LYS 745 and LEU 844. Two salt bridges were seen with LYS 745 and HIS 835 for HB-VPWXE. The hydroxyl group of ring A shows hydrogen bonding with LYS 879, while the C and D rings interact with ASN 842. The peptide part of the conjugate, specifically the tryptophan residue, forms hydrophobic interactions with VAL 726 and LEU 718 while the proline moiety forms hydrophobic interactions with ARG 841 and LEU 799. Interestingly, ARG 841 is a crucial residue that has been shown to be involved in the binding of several lapatinib mimics with wild type EGFR, (Mehmankhah et al. 2014). Additional interactions with HB-VPWXE are also seen with the activation loop residues ASP 855 and ASP 837, which is highly conserved in EGFRs (Gajiwala et al. 2013). For the oleanolate-VPWXE conjugate, hydrophobic interactions are formed between ring A of the oleanolate moiety and TRP 880, while ring D forms hydrophobic interactions with LEU 844. The tryptophan moiety of the oleanolate-VPWXE is once again found to interact with LEU 718 and VAL 726, while the valine moiety interacts with LEU 799. Activation loop residues THR 854 and ASN 842 are also found to interact with the conjugate. Similar interactions were seen for the pentacyclic tri-terpenoid 12, 13 dihydro-alpha amyrin-20, 30-en-3 ol, which showed strong binding with EGFR and inhibited the growth of myeloma cells (Mulyadi 2011). While the perillate conjugate formed interactions with residues in the same region, one notable difference compared to the other conjugates was that binding was observed further into the C-terminal between the prop-1-ene-2-yl group of the perillate moiety with the ALA 1000 residue. The ursolate-VPWXE conjugate interacted with similar residues as the other conjugates, as well as with CYS 797, which was seen for VPWXE. An interaction specific to the ursolate-VPWXE conjugate included the MET 793 residue in the hinge region. Both these residues have been found to be critical for binding with drugs that are considered potent inhibitors such as Osimertinib (Beyett et al. 2022).

PLIP analysis was also conducted to explore the interactions of the designed peptide MEGPSKCCFSLALSH (MFSL) and its conjugates with both the wild type and the double mutant T790M/L858R. For the wild type EGFR, results are shown in Supplementary Information Table S2a and Fig. 5). In the case of MFSL, interactions were seen with the catalytic loop residue ARG 817, with which three H-bonds were formed; as well as with Gly-rich loop residues including PHE 699, ALA 698, SER 696 and GLY 700.

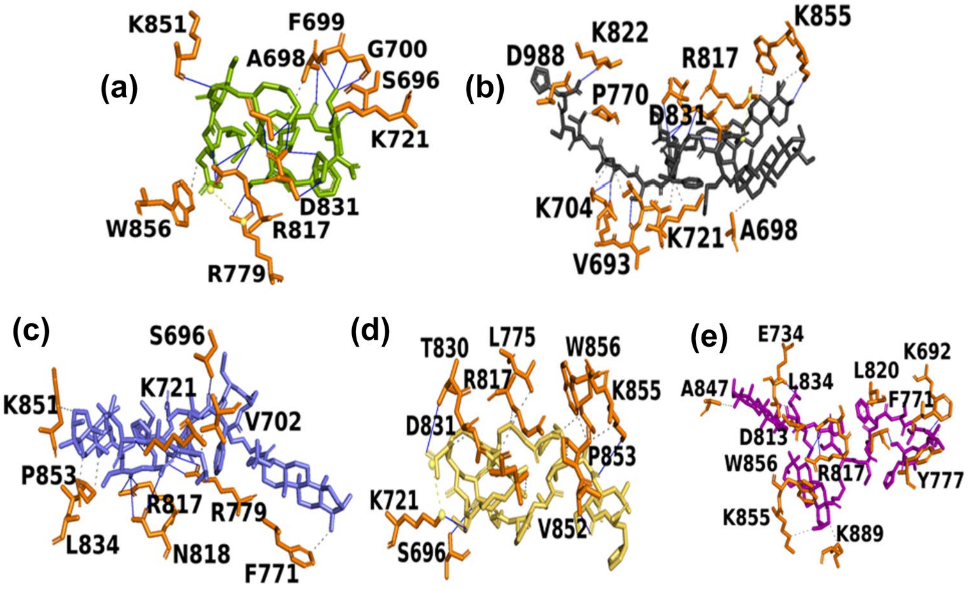

Fig. 5 Binding interactions analysis of MFSL and its conjugates obtained from PLIP with wild type EGFR. **a** MFSL; **b** (HB)2-MFSL; **c** (oleanolate)2-MFSL; **d** (perillate)2-MFSL and **e** (ursolate)2-MFSL

Interactions with the key active site residue ASP 831 of the DFG motif and the activation loop residue LYS 851 were also seen. Interestingly, most interactions were H-bonds, while the only two hydrophobic interactions occurred with ALA 698 and TRP 856. A salt bridge was also formed with ARG 779. The interaction with the DFG motif residue ASP 831 was also seen for the (HB)$_2$-MSFL and the (perillate)$_2$-MFSL conjugate. In addition, H-bond interactions for (HB)$_2$-MFSL included binding pocket residues VAL 693, LYS 692, LYS 604, CYS 773, LYS 822 and ASP 776. The interaction with CYS 773 is particularly interesting to note as it has been an attractive target for some EGFR inhibitors, including a class of compounds that were found to alkylate CYS 773 and irreversibly inactivate the receptor (Fry et al. 1998). As in the case of the VPWXE conjugates, the terpenoid conjugates of MSFL also showed increased hydrophobic interactions. Notable residues included ALA 698, VAL 702, TRP 856, and LYS 721. (HB)$_2$-MFSL also formed a salt bridge with ARG 817 of the catalytic loop. Interestingly, the histidine moiety of the peptide part of the conjugate interacted through hydrophobic interactions with ASP 988. This suggests that the conjugate binds with residues within the ATP binding pocket and extends into the C-terminal residues. The (oleanolate)$_2$-MFSL conjugate and the (perillate)$_2$-MFSL conjugates shared H-bond interactions with SER 696 and LYS 721, though the (oleanolate)$_2$-MFSL conjugate displayed only five hydrophobic interactions compared to nine hydrophobic interactions seen for the corresponding perillate conjugate. Furthermore, the (perillate)$_2$-MFSL conjugate also displayed a salt bridge with the critical residue LYS 721. The catalytic loop residues ARG 817 and ASN 818 formed two hydrogen bonds each with (oleanolate)$_2$-MFSL while ARG 817 formed hydrophobic interactions with the (perillate)$_2$-MFSL conjugate. Additionally, the activation loop residue PRO 853 also formed hydrophobic interactions with both the conjugates. The (ursolate)$_2$-MFSL conjugate showed ten hydrophobic interactions with wild type EGFR, with notable residues including ALA 847 and LEU 834 from the activation loop region, LEU 820 of the catalytic loop region, and LYS 855 and TRP 856, which are allosteric site residues that have been shown to play a critical role in enhancing binding interactions with drugs that target EGFR overexpressed receptors and its mutant (Zhao et al. 2018). H-bonds were also formed with the catalytic loop residues ASP 813 and ARG 817 as well as with the Gly-rich loop region residue LYS 692. While this conjugate did not extend deep into the C-terminal of the receptor, it formed critical interactions with the binding pocket and allosteric sites, which have been shown to interact with several EGFR inhibitors.

We then compared the interactions of the MFSL peptide and its conjugates with the double mutant EGFR T790M/L858R (Supplementary Information Table S2b and Fig. 6). The neat peptide showed 16 hydrogen bonds with the double mutant receptor, while it formed 19 H-bonds with the wild type. The residue PHE 856 formed stacking interactions with the phenylalanine moiety of the peptide in the case of the double mutant receptor, which was promising. Furthermore, for the double mutant receptor, the LYS 745 residue was involved both in H-bond interactions and in hydrophobic interactions with the peptide, specifically with the amide bond of the serine residue of the peptide moiety. This interaction is notable given that the double mutant kinase receptor is known to form a salt bridge between GLU 762 and LYS 745, which is key for its activity (Tamirat et al. 2019). Other interactions included those with THR 854 and ASP

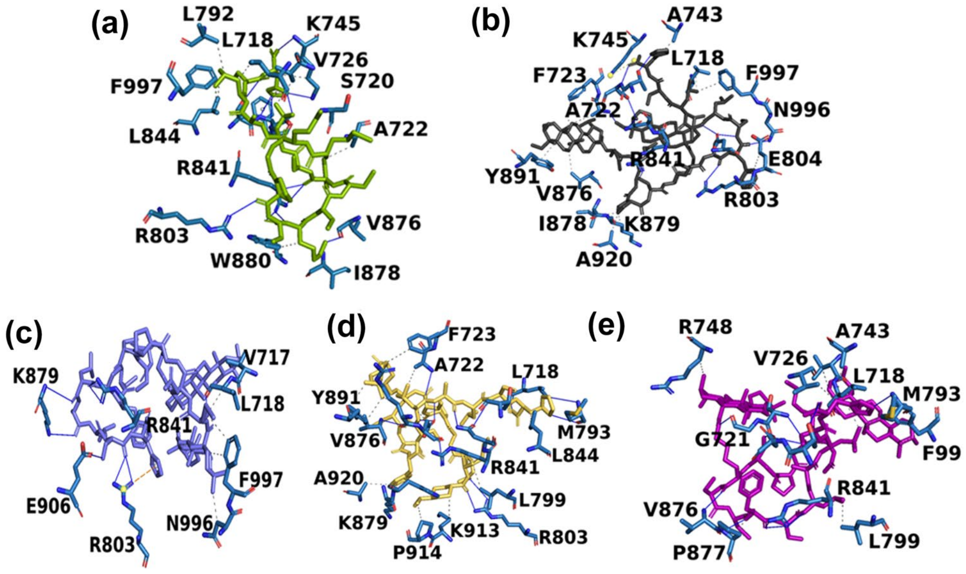

Fig. 6 Binding interactions analysis of MFSL and its conjugates obtained from PLIP with T790M/L858R EGFR. **a** MFSL; **b** (HB)$_2$-MFSL; **c** (oleanolate)$_2$-MFSL; **d** (perillate)$_{2}$-MFSL and **e** (ursolate)$_2$-MFSL

855 and with the activation loop residues LEU 844 and ARG 841. The glutamic acid residue of the peptide was found to interact with VAL 876, ILE 878, and TRP 880. The leucine and alanine residues of the peptide interacted with LEU 718, PHE 997, LEU 844 and with LEU 792.

The interaction with PHE 997 was found to be consistently present for all of the conjugates, with the exception of the (perillate)$_2$-MFSL conjugate. PHE 997 is part of the C-terminal tail β-strand that tracks the surface of the kinase domain, and is close to the AP2 helix of EGFR (Martin-Fernandez et al. 2019). In recent work, it was shown that molecules such as 1,2,3-triazole tethered chalcone derivatives were found to interact with PHE 997 and LYS 745 and exhibited high docking scores with EGFR and potent inhibitory activity against breast and cervical tumor cells (Gurrapu et al. 2020). Overall, the highest number of hydrophobic interactions was seen for (perillate)$_2$-MFSL at fourteen, while (oleanolate)$_2$-MFSL only showed six hydrophobic interactions. Key residues for the (oleanolate)$_2$-MFSL conjugate to interact within the binding pocket included LEU 718, ARG 841, and VAL 717. ARG 803 formed a pi-cation interaction with the histidine component of the peptide moiety of the conjugate while both PHE 997 and ASN 996 were involved in hydrophobic interactions with the conjugate.

A unique interaction specific for the (oleanolate)$_2$-MFSL conjugate was a single H-bond with GLU 906, while (perillate)$_2$-MFSL displayed distinctive interactions with PRO 914 and LYS 913. Key interactions included those with the hinge region residues MET 793 as well as LEU 799 and activation loop residues ARG 841 and LEU 844. Interactions were also seen with Gly-rich P-loop residues LEU 718 and ALA 722 which has been implicated in binding to EGFR T790M/L858R based inhibitors (Kovacs et al. 2015). (HB)$_2$-MFSL showed equal numbers of H-bond interactions and hydrophobic interactions (twelve each), with key residues similar to those mentioned above within the binding pocket. The B and C rings of the terpenoid parts of the conjugate interacted with TYR 891, VAL 876, ALA 722 and PHE 723 through hydrophobic interactions while all other interactions occurred with the peptide segment of the conjugate. These included residues from the C-terminal tail such as ASN 996 and PHE 997 as well as those within ATP binding cleft, ALA 743 and LYS 745, among other residues. Hydrophobic interactions with PHE 723 in particular are promising as it has been implicated in the binding interactions of several EGFR (T790M/L858R) inhibitors (Agarwal et al. 2022). Thus, (HB)$_2$-MFSL also showed strong interactions with key residues within the binding pocket. Likewise, notable interactions were also seen with the (ursolate)$_2$-MFSL conjugate with hinge region residues MET 793 and LEU 799 as well as with LEU 718 and VAL 726, which are known to be critical for ligand independent dimerization of the double mutant receptor (Zhu et al. 2018). Thus, based on the docking studies overall, it appears that the terpene conjugates were able to bind successfully to both the wild type EGFR and the EGFR T790M/L858R double mutant, though different regions of the binding pocket residues were involved.

Among the neat terpenoids, (Supplementary Information Table S3 and Fig. S1) oleanolic acid and ursolic acid did not show any H-bond interactions with the T790M/L858R EGFR receptor, while perillic acid and hydroxybetulinic acid displayed two hydrogen bonds each. The neat terpenoids, however, did display hydrophobic interactions with binding pocket residues, including those with residues from the activation loop. Hydroxybetulinic acid showed interactions with TRP 880, LYS 879, and PRO 877, implying that it binds with residues further into the C-terminal of the double mutant receptor. In comparison, hydroxybetulinic acid showed seven hydrophobic interactions with the wild type EGFR receptor, among which involved the residues LYS 721 and LEU 694. Additionally, a H-bond with the DFG motif residue ASP 831 was observed. Comparatively, perillic acid and ursolic acid showed significantly fewer interactions with the wild type receptor. Only three hydrophobic interactions were formed with perillic acid and two hydrogen bonds and one hydrophobic interaction were formed with ursolic acid. Oleanolic acid formed a H-bond with MET 769 and four hydrophobic interactions with residues from the hinge region and the catalytic loop region. These results imply that conjugation with both peptides significantly enhances the binding interactions with the receptors.

Molecular Dynamics

To investigate the stability and to further elucidate the differences in binding of the conjugates within the binding pockets of wild type EGFR and EGFR T790M/L858R, we conducted the molecular dynamics (MD) simulations. Given that more interactions were seen with the peptides and the conjugates, MD simulations were conducted for the peptides and the conjugates. A comparison of the RMSD values obtained for T790M/L858R and the wild type EGFR receptor is shown in Table 4. Overall, the lowest RMSD values for the wild type receptor complexes were seen for the (ursolate)$_2$-MFSL conjugate and the neat MFSL peptide, followed by the ursolate-VPWXE conjugate complex. All other conjugates demonstrated RMSD values between 0.39 and 0.55 nm, which were also indicative of fairly stable binding in all cases. For the double mutant receptor, however, the RMSD values were marginally higher in all cases with the exception of the (oleanoate)$_2$-MFSL conjugate complexed with the T790M/L858R receptor. This complex showed the lowest RMSD value with the double mutant (0.31 nm). All of the other MFSL-terpene conjugate complexes also showed low RMSD values ranging between 0.34 and 0.39 nm. The neat MFSL peptide showed a higher RMSD value with double mutant receptor compared to the wild type, indicating that it formed a more stable complex with the wild type. Interestingly, the oleanoate-VPWXE conjugate complex with the T790M/L858R double mutant receptor showed the highest RMSD value (0.88 nm) and thereby is indicative of lowest stability among all conjugates and peptides, followed by the HB-VPWXE conjugate complex at 0.74 nm with the double mutant receptor.

To further illustrate the differences in binding interactions and investigate the binding mechanism with the receptors, we examined the trajectories (Fig. 7). A comparison of the HB-VPWXE conjugates reveals that, in the case of the wild type, the conjugate undergoes slight conformation changes during the simulation while still largely remaining confined to the binding pocket, making contacts mostly with the P-loop, as well as the C-helix and the beta3/αC residues. For the double mutant, however, major changes occur in the conformation of HB-VPWXE. Initially, binding occurs within the ATP binding cleft while the rings of the terpenoid component of the conjugate are seen interacting with the C-lobe alpha-helices. However, by 50 ns, there is a change in position of the terpenoid component of the conjugate, and as it moves toward the ATP binding cleft, it continues to interact with ARG 841 of the activation loop. By 100 ns, it moves further into the binding cleft, making contacts with αC-β4 loops, while interacting with activation loop residues ASP 837 and ASP 855. Throughout the simulation, it remains in contact with the LYS 745 residue, which is a key residue within the active site as previously mentioned. Changes are also seen in the conformation of the C-helix. This would explain the higher RMSD values seen for the HB-VPWXE with the double mutant.

In the case of the wild type receptor, the oleanoate-VPWXE conjugate also remains confined within the binding cleft throughout the simulation, with the TRP moiety of the peptide moving further toward the catalytic loop, making

Table 4 Average RMSD values obtained upon complexation of VPWXE and MEGPSKCCFSLALSH (MFSL) and their conjugates with EGFR (wild type) and double mutant (T790M/L858R)

	EGFR (Wild Type)		EGFR (T790M/L858R)	
	Cα RMSD (nm)	P-L RMSD (nm)	Cα RMSD (nm)	P-L RMSD (nm)
VPWXE	0.326	0.504	0.266	0.480
HB-VPWXE	0.195	0.393	0.279	0.743
Oleanoate-VPWXE	0.260	0.509	0.215	0.883
Perillate-VPWXE	0.226	0.552	0.260	0.597
Ursolate-VPWXE	0.336	0.376	0.253	0.485
MEGPSKCCFSLALSH (MFSL)	0.354	0.291	0.407	0.386
(HB)$_2$-MFSL	0.396	0.552	0.338	0.342
(oleanolate)$_2$-MFSL	0.304	0.493	0.343	0.313
(Perillate)$_2$-MFSL	0.315	0.432	0.325	0.390
(ursolate)$_2$-MFSL	0.315	0.296	0.389	0.347

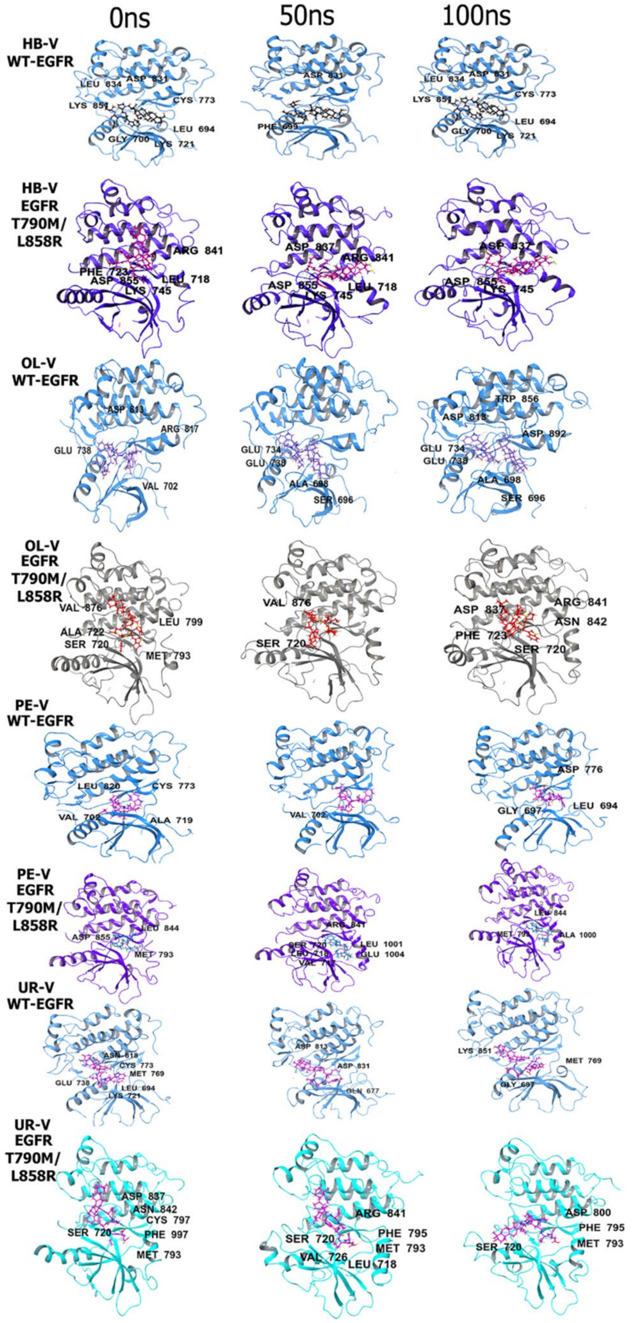

Fig. 7 Comparison of trajectory snap shots at 0 ns, 50 ns, 100 ns of VPWXE peptide conjugates with wild type and T790M/L858R EGFR. *WT* Wild Type, *V* VPWXE, *HB* hydroxybetulinate, *OL* oleanolate, *PE* perillate, *UR* ursolate

contact with the ASP 813 residue by the end of the simulation. Furthermore, the conjugate appears to spread out into the binding cleft of the wild type receptor over the course of the simulation. On the other hand, the opposite behavior is seen for the conjugate with the double mutant receptor during the course of the simulation where, initially, the conjugate is spread out, interacting with both N-lobe and C-lobe residues as well as the hinge region. However, by the end of the simulation, it becomes more compact and folds up on itself, primarily making contact within the binding cleft residues such as ASP 837 and PHE 723, among others.

The perillate-VPWXE conjugate also shows binding interactions within the binding cleft of the wild type receptor with few changes over the course of the simulation as the conjugate becomes more compact. However, the conjugate appears to change positions and move further into the C-terminal tail region containing residues LEU 1001, ALA 1000, and GLU 1004 over the course of the simulation when complexed with the double mutant receptor. Interestingly, the interaction with the key hinge region residue MET 793 is lost temporarily at 50 ns, but it is restored by the end of the simulation. The terpenoid component appears to move toward the C-lobe, while the peptide component is seen interacting more within the ATP binding cleft region. For the wild type, the trajectories over 100 ns for the ursolate-VPWXE complex shows that the conjugate remains constricted within the binding cleft, with slight changes in the conformation of the conjugate. Key interactions with hinge region residues and activation loop residues are seen throughout the course of the simulation, which explains its low RMSD values. In the case of the double mutant receptor, however, ursolate-VPWXE appears to change its position during the course of the simulation, where most interactions are initially seen with the C-lobe residues and the hinge region residues. However, by the end of the simulation, the conjugate appears to move further into the loop regions within the binding cleft. Of note is the fact that its interaction with MET 793 remains throughout the simulation.

The peptide VPWXE alone (Supplementary Information Fig. S2) is initially seen interacting with LYS 721, the DFG motif residue ASP 831, LYS 851 of the activation loop and ARG 817 of the catalytic loop of the wild type receptor. However, over the course of simulation, interactions are seen with the Gly-rich P-loop residues PHE 699 and GLY 700 along with the hinge region residue MET 769. Additional interactions are also seen with CYS 773 and THR 830. In comparison, for the double mutant complexed with VPWXE, although a number of interactions with key residues such as MET 793, MET 790, ASP 855, ASP 837, CYS 797 occur in the first 50 ns of the simulation, the number of interactions reduces over the course of simulation, with only one interaction with ASP 855 remaining at the end of the simulation. Thus, it appears that neat VPWXE has a stronger and more stable interaction with the wild type EGFR compared to the double mutant receptor over the course of the simulation.

A comparison of the trajectories of the MFSL conjugates are shown in Fig. 8. As shown, for the wild type receptor complexed with $(HB)_2$-MFSL, the conjugate occupies the binding pocket and extends into the N-lobe and C-lobe

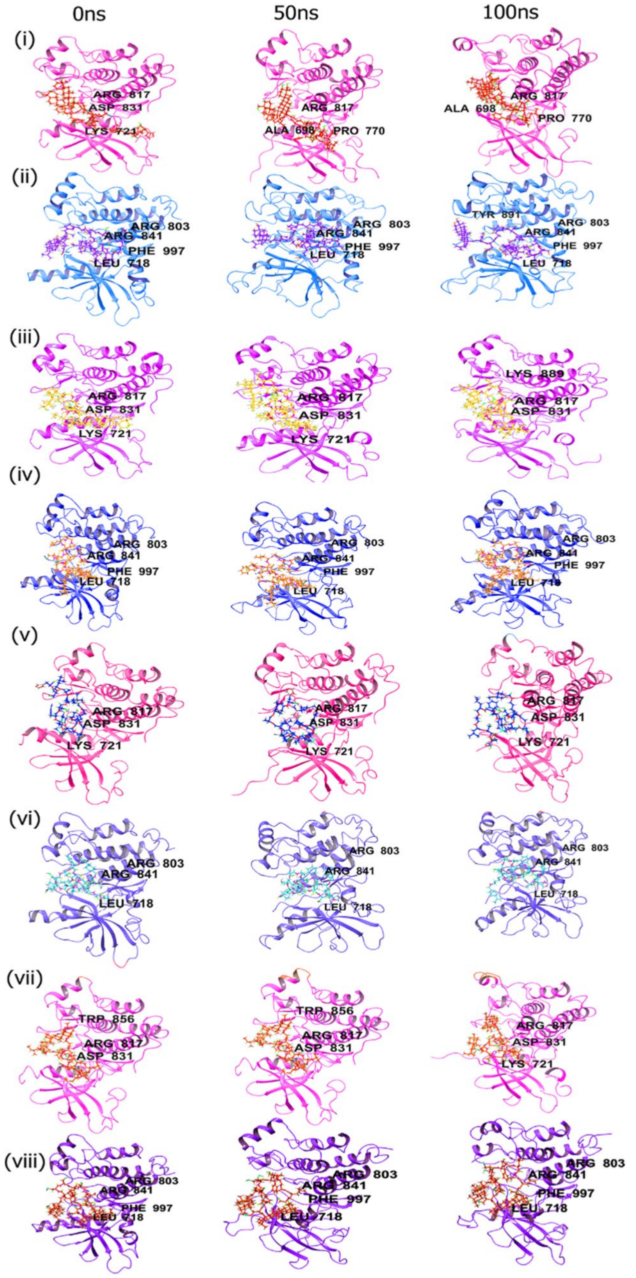

Fig. 8 Trajectory snapshots of MFSL conjugates over 100 ns simulations. (i & ii) $(HB)_2$-MFSL with WT EGFR and T790M/L858R respectively; (iii & iv) $(Oleanolate)_2$-MFSL with WT EGFR and T790M/L858R respectively; (v & vi) $(perillate)_2$-MFSL with WT EGFR and T790M/L858R respectively; $(ursolate)_2$-MFSL with WT EGFR and T790M/L858R respectively. WT = wild type

residues. Furthermore, over the course of the simulation, the entire conjugate continues to remain within the binding pocket, making contacts with ALA 698 of the P-loop region, ARG 817 of the catalytic loop, and PRO 770. In the case of the T790M/L858R receptor, however, the terpene part of the conjugate appears to completely move out of the binding pocket by 100 ns, though, the peptide portion remains within the pocket and interacts with the C-terminal residues (PHE 997). This contributes to the relatively higher RMSD value for the $(HB)_2$-MFSL conjugate, with the double mutant receptor. In comparison, the $(oleanolate)_2$-MFSL conjugate appears to remain tightly bound to the double mutant receptor over the course of the entire simulation and interacts with the activation loop residue ARG 844, as well as LEU 718 and ARG 803. The peptide component of the conjugate extends deep into the C-lobe, making contact with the PHE 997 residue. Thus, unlike $(HB)_2$-MFSL, the $(oleanolate)_2$-MFSL conjugate forms a highly stable complex with the double mutant receptor. This can be attributed to the structural differences between HB and oleanolate. While oleanolate contains 5 six membered rings, which may allow for more hydrophobic interactions, HB contains 4 six membered rings and one five membered ring, as well as an additional $–CH_2OH$ group attached to ring A. The additional hydroxyl group may contribute further H-bond interactions with the receptor.

The $(oleanoate)_2$-MFSL also forms a tightly bound complex with the wild type receptor. Although there is an initial change in conformation of $(oleanolate)_2$-MFSL, after 50 ns, very little change is observed overall. Furthermore, $(oleanolate)_2$-MFSL remains in contact with the activation loop throughout the course of the simulation. While it also interacts with LYS 721 for the first 50 ns, this interaction is not seen at the end of the simulation. Instead, a new interaction with LYS 889 appears, which suggests that the conjugate moves further into the C-lobe by the end of the simulation.

Interestingly, in the case of the $(perillate)_2$-MFSL conjugate, the -Leu-Ser-His residues, which belong to the C-terminal portions of the peptide part of the conjugate appeared to be outward of the binding pocket of the wild type receptor, while the perillate ring components of the conjugate along with the rest of the peptide folded into the binding pocket, interacting with the DFG motif residue ASP 831, as well as with LYS 721 and ARG 817. Overall, the conjugate did not undergo major changes in position during the simulation, accounting for its low RMSD value. Interestingly, this conjugate behaves slightly differently when complexed with the double mutant receptor, where initially, the entire conjugate fits into the binding pocket and also interacts with the C-lobe residues. However, it then spreads out over the course of the simulation into the C-helix, which is in proximity with the N-lobe. Key interactions with LEU 718, ARG 803, and ARG 801 remain consistent throughout the simulation. Thus, this conjugate shows stable binding with both the double mutant and wild type receptor.

The $(ursolate)_2$-MFSL conjugate formed a stable complex with the wild type receptor as confirmed by the trajectory images that show interactions with the DFG motif and with LYS 721 of the G-rich P-loop. Additionally, an interaction with ARG 817 formed toward the end of the simulation, which remained consistent, particularly between 50 and 100 ns. The (ursolate)$_2$-MFSL conjugate, when complexed with the double mutant receptor EGFR T790M/L858R, was found to form an even more stable complex with the entire conjugate, remaining tightly attached to the binding pocket throughout the course of the simulation. In addition to ARG 841, LEU 718, and ARG 803 residues, this conjugate also interacted with the C-terminal region residue PHE 997. Thus, the (ursolate)$_2$-MFSL formed the most stable complex with the T790M/L858R receptor among the MFSL conjugates. The neat MFSL also interacted favorably within the binding pocket of the T790M/L858R double mutant receptor, (Supplementary Information Fig. S3) though the peptide itself underwent conformation changes during the simulation process. Furthermore, it interacted with key residues including LEU 718, PHE 997, ARG 803 and ARG 841 throughout the simulation. Comparatively, the neat MFSL interacted with only three residues during the simulation process with the wild type receptor, specifically with residues LYS 721, ARG 817, and ASP 831, all of which have been implicated in regulation of kinase activity. The peptide remained bound to the binding pocket throughout the simulation. Thus, overall, these results indicate that most of the MSFL-triterpenoid conjugates were found to remain in contact not only within the ATP binding pocket region but also with allosteric regions and the C-terminal tail portion of the double mutant receptor, while in the case of the wild type receptor, fewer interactions were observed with the C-terminal portion of the receptor.

Radius of Gyration

The radius of gyration provides information about the compactness of the structure within the receptor complex (Minnelli et al. 2020). Results are shown in Fig. 9. For the wild type receptor, on average, the radius of gyration of VPWXE and its conjugates appeared to be lower than MFSL and its conjugates. This is expected given the size of the MFSL peptide, which is a longer peptide segment and therefore is more flexible. Additionally, for each conjugate, MFSL is conjugated to two terpenoid moieties, while VPWXE conjugates are attached to one terpenoid moiety. The peptide VPWXE and perillate-VPWXE formed more compact structures as expected, as the perillate has a single hydrophobic ring, compared to the pentacylic terpene conjugates that folded up over time during the simulation. No changes or fluctuations were observed in general, with the exception of oleanolate-VPWXE, in which case for the first 15 ns of the simulation, the rGyr value increased, but then, it decreased to 0.67 nm and was able to maintain a steady value of 0.68 nm for the rest of the simulation. The rGyr remained steady and displayed a relatively constant value (< 0.05 nm change) throughout the simulation for all of the other VPWXE conjugates.

Amongst the MFSL conjugates however, the rGyr values showed changes throughout the simulation for the (HB)$_2$-MFSL conjugate. By the end of the simulation, the rGyr value stabilized at 1.1 nm, implying that (HB)$_2$-MFSL formed the least compact structure within the receptor which corroborates with the trajectories. The (ursolate)$_2$-MFSL conjugate had the second highest value among the MFSL conjugates within the wild type receptor. However, the value remained relatively constant throughout the simulation. This implies that the conjugate is more spread out within the receptor but does not undergo changes in conformation once complexed with the receptor. The (oleanolate)$_2$-MFSL conjugate also showed a similar trend as the ursolate counterpart, indicating that it also underwent very few changes within the receptor and formed a slightly more compact

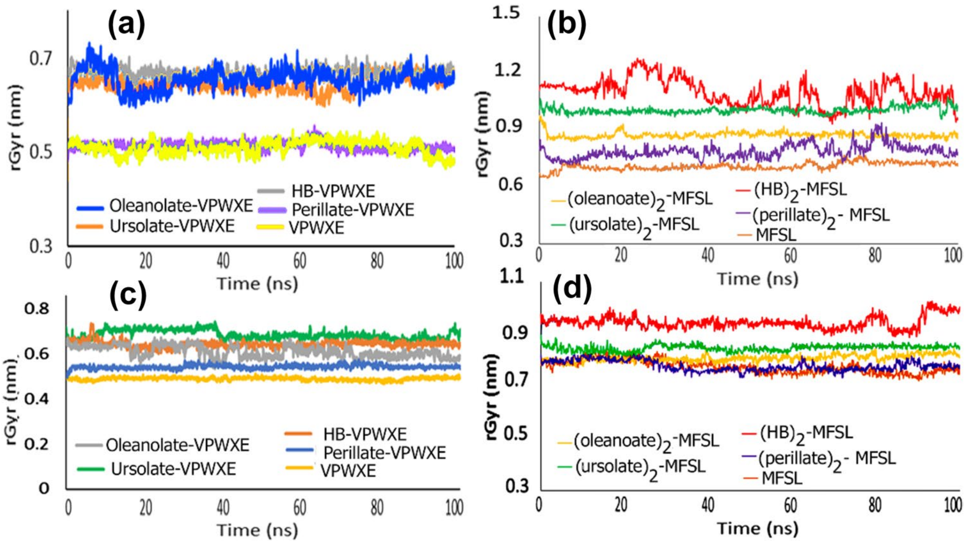

Fig. 9 Comparison of radius of gyration of **a** VPWXE and its conjugates complexed with wild type EGFR; **b** MFSL and its conjugates complexed with wild type receptor. **c** VPWXE and its conjugates complexed with EGFR T790M/L858R receptor; **d** MFSL and its conjugates complexed with EGFR T790M/L858R

structure compared to (ursolate)$_2$-MFSL. The neat peptide showed the lowest rGyr values, while the (perillate)$_2$-MFSL conjugate showed a slightly higher rGyr value compared to the neat peptide, and displayed fluctuations between 50 and 82 ns during the simulation, after which it stabilized at 0.75 nm.

For the EGFR T790M/L858R double mutant receptor, the VPWXE and its peptide conjugates showed a similar trend as that of the wild type receptor. Average values varied between 0.5 and 0.75 nm. All of the conjugates showed very few changes during the course of the simulation with the exception of oleanolate-VPWXE, which showed minuscule change between 30 and 45 ns, after which it maintained a steady value of 0.62 nm for the rest of the simulation. Ursolate-VPWXE showed a marginal increase in rGyr between 15 and 40 ns, after which it stabilized at 0.71 nm for the rest of the simulation. For the MFSL conjugates, the average rGyr value was found to be between 0.82 and 0.85 nm, with very little fluctuation in most cases; an exception being the (HB)$_2$-MFSL conjugate, which showed a higher rGyr value at 1.0 nm. A slight decrease was seen between 80 and 90 ns, after which the value once again increased to 1.05 nm and remained constant. Thus, the (HB)$_2$-MFSL conjugate formed the least compact structural complex with both the wild type and the double mutant receptor. Furthermore, MFSL conjugates showed slightly higher values on average with the double mutant receptor compared to the wild type. Overall, most complexes did not show fluctuations in structures and remained relatively compact throughout the simulation.

MMGBSA Studies

The binding energies of the conjugate and the peptide complexes over the course of the simulation were obtained using MMGBSA. This provides an accurate evaluation of the free energies for binding of each of the ligands over the course of the entire simulation (Suenaga et al. 2012). Results obtained are shown in Table 5. As can be seen for the wild type EGFR, among the conjugates, the highest binding energy was found for the (ursolate)$_2$-MFSL conjugate at – 115.69 kcal/mol, followed by ursolate-VPWXE and oleanolate-VPWXE at – 87.87 kcal/mol and – 87.50 kcal/mol respectively. Interestingly, in the case of the (ursolate)$_2$-MFSL conjugate, the largest contribution came from the Van der Waals interactions. However, for both oleanolate-VPWXE and ursolate-VPWXE, the major contribution was from electrostatics energy. This suggests that the binding modes and residues within the receptor were different for the VPWXE conjugates compared to the MFSL conjugates, which corroborates with the molecular dynamics studies

Table 5 MMGBSA analysis

	Average ΔG binding energy	Average electrostatic energy	Average H-bond energy	Average lipophilic energy	Average Van der Waals energy
Wild Type EGFR					
VPWXE	– 93.81	– 264.27	– 9.89	– 17.36	– 59.13
HB-VPWXE	– 74.59	– 225.93	– 880	– 13.73	– 49.48
Oleanolate-VPWXE	– 87.50	– 238.73	– 10.01	– 16.37	– 55.74
Ursolate-VPWXE	– 87.87	– 237.97	– 9.37	– 16.02	– 58.77
Perillate-VPWXE	– 77.11	– 200.87	– 8.69	– 14.98	– 53.89
MEGPSKCCFSLALSH (MFSL)	– 66.61	– 27.06	– 3.61	– 15.15	– 71.82
(HB)$_2$- MFSL	– 80.54	– 45.38	– 2.93	– 17.55	– 83.62
(Oleanolate)$_2$-MFSL	– 72.54	– 35.43	– 3.12	– 20.49	– 79.09
(Perillate)$_2$-MFSL	– 51.46	– 10.13	– 1.47	– 12.95	– 65.02
(Ursolate)$_2$-MFSL	– 115.69	– 34.93	– 3.52	– 28.81	– 113.06
T790M/L858R EGFR					
VPWXE	– 57.77	– 8.55	– 1.93	– 13.71	– 55.73
Hydroxybetulinate-VPWXE	– 78.39	– 41.31	– 3.46	– 21.98	– 69.90
Oleanolate-VPWXE	– 48.88	– 22.29	– 2.05	– 14.06	– 44.77
Ursolate-VPWXE	– 77.34	– 29.76	– 1.89	– 21.82	– 65.64
Perillate-VPWXE	– 66.41	– 14.58	– 1.456	– 19.28	– 57.95
MEGPSKCCFSLALSH (MFSL)	– 96.05	– 329.45	– 9.69	– 22.81	– 69.97
(HB)$_2$- MFSL	– 87.35	– 34.18	– 3.87	– 22.69	– 90.54
(Oleanolate)$_2$-MFSL	– 59.29	– 28.74	– 2.84	– 16.99	– 64.21
(Perillate)$_2$-MFSL	– 83.24	– 296.24	– 10.11	– 21.51	– 71.09
(Ursolate)$_2$-MFSL	– 78.14	– 29.22	– 2.60	– 19.08	– 71.61

(Zhang et al. 2017). Neat VPWXE showed a higher ΔG bind (− 93.81 kcal/mol) compared to the MFSL peptide for the wild type, which displayed a ΔG bind of − 66.61 kcal/mol.

For the T790M/L858R receptor, however, the highest ΔG binding energy was seen for the MFSL peptide at − 96.05 kcal/mol, while VPWXE showed a binding energy of − 57.77 kcal/mol. Thus, the two peptides display opposite behavior with the two receptors, which is likely because of the structural changes that occur within the double mutant receptor and therefore each of these may impart specificity (Lowder et al. 2015). As was seen in most cases, during the simulation, the MFSL peptide and its conjugates appeared to interact not only with the binding cleft but into the C-terminal residues of the receptor, which was not the case for the VPWXE conjugates. Among the conjugates, the $(HB)_2$-MFSL conjugate showed the second highest binding energy at − 87.35 kcal/mol followed by $(perillate)_2$-MFSL at − 83.24 kcal/mol and $(ursolate)_2$-MFSL at − 78.14 kcal/mol. Overall, it appears that most of the VPWXE conjugates had higher binding energies with the wild type receptor, while the MFSL conjugates displayed higher ΔG_{bind} with the double mutant, with the exception of the oleanolate conjugates which showed an opposite trend.

Molecular Surface Area (MolSA)

The MolSA value is representative of the Van der Waals surface area, which was calculated using a 1.4 A^0 probe radius for all simulations (Rashid et al. 2022). Results obtained are shown in Supplementary Information Fig. S4. As can be seen, for the wild type receptor, the MolSA values were found to be higher for the MFSL peptide and its conjugates compared to the VPWXE peptide and its conjugates. Significantly higher MolSA values were seen for $(HB)_2$-MFSL, $(ursolate)_2$-MFSL, and $(oleanolate)_2$-MFSL conjugates (between 160 and 180 nm^2) compared to $(perillate)_2$-MFSL and the peptide alone (110 and 130 nm^2) respectively. However, in the case of the $(perillate)_2$-MFSL conjugate, the MolSA value appeared to increase over the course of the simulation. This corroborates with the results obtained for the MMGBSA, which showed a higher contribution of the Van der Waals forces for MFSL and its conjugates in binding with the receptor compared to the VPWXE conjugates. In general, the lower the MolSA value, the more stable the protein–ligand complex and vice-versa (Ferdausi et al. 2022). Thus, VPWXE and its conjugates, which showed lower MolSA values, appear to form relatively more stable with the wild type receptor. This can also be attributed to the size of the conjugates, which was larger for the MFSL peptide and its conjugates.

For the T790M/L858R double mutant, a similar trend was observed. However, the perillate-VPWXE showed an increase in the first 5 ns, after which it showed a stable value (68.3 nm^2) for the rest of the simulation. Thus, the perillate-VPWXE had a slightly higher value for the double mutant complex compared to the wild type. All of the other conjugates showed MolSA values in a similar range as that of the wild type receptor. As with the wild type receptor, the MolSA values for the MFSL peptide and its conjugates were higher for the double mutant receptor and values obtained were in a similar range as the wild type, indicating that the Van der Waals forces involved in binding of those conjugates were comparable for both the wild type and double mutant receptor.

Based on the computational results, as a proof of concept, we synthesized and self-assembled three of the triterpenoid conjugates with MFSL and VPWXE peptides to prepare nanoassemblies. We further examined their interactions with wild type EGFR as well as the T790M/L858R double mutant receptor expressing cell lines.

Growth and Morphological Study of Nanoassemblies

Each of the conjugates were allowed to self-assemble over a period of 2 weeks. The growth of the assemblies was monitored using dynamic light scattering (Supplementary Information Fig. S5). As can be seen, the oleanolate-VPWXE nanoassemblies were found to be monodisperse and within a size range of 150–200 nm. In comparison, the corresponding MFSL conjugate nanoassemblies overall were found to be bigger in size (average of 1 µm) and were polydisperse. The VPWXE conjugate of HB displayed a size range of 1 µm to 3 µm, while a trimodal distribution was observed for the corresponding MSFL conjugates, indicating that nanoassemblies varied in size. The assemblies formed for the ursolate-VPWXE conjugates showed a single peak at 3000 nm, while a bimodal distribution was observed for the corresponding MFSL conjugate which showed a bimodal distribution with more assemblies in the sizes range of 1 µm and a small number of assemblies in the range of 5 µm. The larger sizes may be due to possible aggregation of the nanoassemblies that occurred over time.

The morphologies of the assemblies obtained was examined by atomic force microscopy (AFM) and scanning electron microscopy (SEM). Results obtained are shown in Fig. 10. The ursolate-VPWXE conjugate formed nanospheres, which appeared to serve as nuclei for the formation of nanochain structures that are formed as the nanospheres diffuse together. This is also corroborated by the corresponding SEM image. The $(ursolate)_2$-MFSL conjugate on the other hand formed fibrillar structures upon self-assembly as shown in the AFM image. The corresponding SEM image shows aggregates, which explains the broader size range observed in the DLS analysis. Similar distribution has been observed upon self-assembly of amphiphilic peptide-heterodimers (Luo et al. 2010) comprised of surfactant mimics

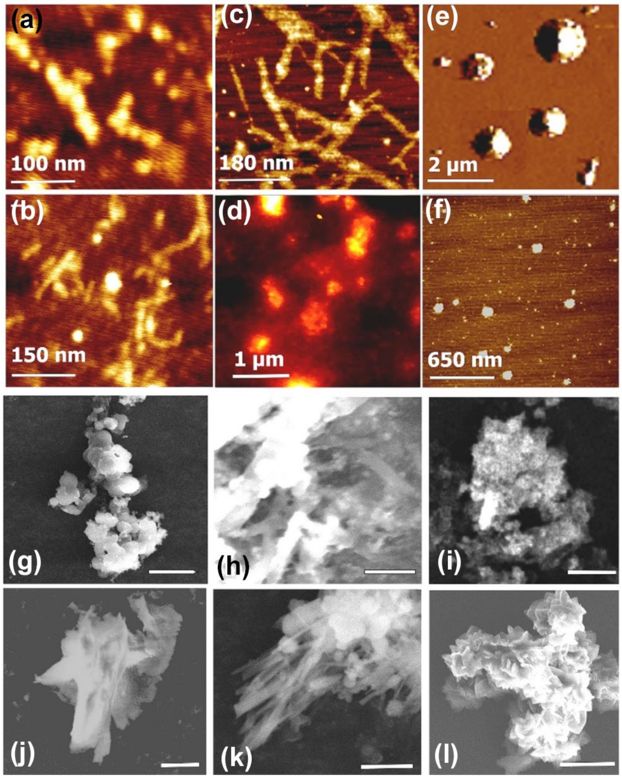

Fig. 10 Top two rows: AFM images of nanoassemblies formed after self-assembly of peptide conjugates after 2 weeks of growth. **a** ursolate-VPWXE; **b** (ursolate)$_2$-MFSL; **c** HB-VPWXE; **d** (HB)$_2$-MFSL; **e** oleanolate-VPWXE; **f** (oleanolate)$_2$-MFSL. Bottom two rows: SEM images: **g** ursolate-VPWXE; (h) HB-VPWXE; **i** oleanolate-VPWXE; **j** (ursolate)$_2$-MFSL; **k** (HB)$_2$-MFSL; **l** (oleanolate)$_2$-MFSL. Scale bar for SEM = 1 μm

with two tail peptide motifs containing $A_6Z_2G_6$ structures, where Z is a charged residue (either K or D). Interestingly, however, largely multi-layered supramolecular structures ranging from spheres to rods were formed for the corresponding for the HB-VPWXE and (HB)$_2$-MFSL conjugate as shown by both the AFM and the SEM images. The nanofibers obtained from the HB-VPWXE conjugates were marginally larger (~30 nm) in diameter compared to the nanorod like structures seen for the (HB)$_2$-MFSL conjugates. In case of the oleanolate-VPWXE conjugates, however, multilayered spherical structures were seen, which were approximately 500 nm to 1 μm in diameter. On the other hand, the (oleanolate)$_2$-MFSL conjugates self-assembled into multilayered nanoplatelet structures which is more evident from the SEM images.

The differences in morphologies can be attributed to the differences in interactions between the conjugate structures. In previous work, triterpenoids such as oleanolic acid have been shown to self-assemble into nanovesicle-like structures, promoted by intermolecular H-bonding involving the carboxyl and hydroxyl groups as well as hydrophobic interactions of the nonpolar triterpenoid backbone (Bag and Paul 2012). In the case of the oleanolate-peptide conjugates studied here, it is likely that the –C=O- - -NH– interactions between the peptide backbones also play a key role in the assembly. In addition, hydrophobic interactions also play a significant role in the self-assembly of the oleanolate-VPWXE conjugate, given that the peptide component is also primarily hydrophobic with the exception of the terminal glutamic acid group, which makes the conjugate amphiphilic. The C-terminal glutamic carboxyl groups of the VPWXE component contribute to H-bonding interactions with the hydroxyl group of oleanolate moiety. The (oleanolate)$_2$-MFSL conjugate is rendered amphiphatic due to the hydrophobicity of the triterpenoid rings and the presence of hydrophobic amino acids (such as leucine, proline, alanine and phenylalanine). In contrast, the presence of serine, glutamic acid and histidine groups contribute to hydrophilicity. The terminal histidine moiety can also participate in intra-molecular pi-cation interactions with the phenylalanine moiety of the conjugate (Liao et al. 2013) and its carboxyl group contributes to H-bonding.

Ursolic acid and oleanolic acid are similar in chemical structure. However, there is a change in the position of one methyl group on ring E in ursolic acid compared to oleanolic acid. This difference has been shown to cause variations in biological activities of the two triterpenoids (Ovesná et al. 2006) and potentially, in the self-assembly process. In previous work, ursolic acid has been shown to self-assemble into membranous fibrillar structures as well as nanospheres in aqueous solutions (Bag et al. 2017). In the case of the (ursolate)$_2$-MFSL and ursolate-VPWXE conjugates, it is likely that formation of hierarchical tubular or nanochain-like structures is thermodynamically more favorable under the conditions studied. The formation of nanofibrillar structures of HB-VPWXE is largely due to hydrophobic interactions and is also likely to be more favorable thermodynamically. This promotes the oligomerization process into the formation of nanofibers. In the case of the (HB)$_2$-MFSL conjugate, thicker fibrils are formed, likely due to the larger peptide sequence and 2 HB moieties that promote more amide group H-bonding and hydrophobic interactions. These results indicate that each of the conjugates formed nanostructures of varying shapes and sizes, which could potentially be applicable in a multitude of biological applications such as drug delivery and biosensing.

NTA Analysis

NTA analysis exhibits the relationship of the Brownian motion of nanoparticles to their hydrodynamic radius in solution (Filipe et al. 2010). In previous work it has been demonstrated that it is also plausible to examine in structural organization of proteins in complex systems through NTA analysis (Juul-Madsen et al. 2021). In this study, we utilized NTA to characterize the nanoassemblies of the tri-terpene peptide conjugates in solution (Fig. 11). The movement of the particles was tracked by particle scattering through a projected laser light source at 488 nm. For the HB-VPWXE assemblies, the size distribution of the detectable particles showed a broad peak, with the largest peak near 225 nm (Fig. 11a), with smaller peaks seen in 600–800 nm range. The HB-MFSL nanoassemblies (Fig. 11b) also displayed a broad peak, with the largest peak at 200 nm and second largest peak seen at 150 nm. Once again, small peaks were seen at 650 nm, 790 nm and at 920 nm, signifying a small percentage of assemblies of larger diameter, likely due to the formation of larger oligomers.

The size distribution of the oleanolate-VPWXE assemblies (Fig. 11c) showed two peaks with similar heights at 150 nm and at 170 nm, along with peaks at 245 nm and at 310 nm. On the other hand, the oleanolate-MFSL nanoassemblies (Fig. 11d) displayed two major peaks at 150 nm and at 204 nm. For the ursolate-VPWXE nanoassemblies multiple peaks were observed at 65 nm, 146 nm, 119 nm, 230 nm and at 183 nm with the highest percentage seen for the 65 nm peak. The ursolate-MFSL nanoassemblies showed major peaks at 80 nm, 113 nm, 190 nm, 250 nm and 304 nm along with shorter peaks in the 400 nm to 600 nm range as well as a short peak at 750 nm. These results are indicative that each of the assemblies formed aggregated species of a variety of sizes and shapes, ranging from small aggregates, intermediate sized assemblies to larger oligomers. These results indicate that assemblies within 1 μm size were detectable by the NTA for all of the tri-terpene conjugates with the hydrodynamic sizes showing agreement with results seen from AFM analysis in most cases. However, it is likely that the larger aggregates are not detected by NTA.

Cell Studies

We examined the interactions of the nanoassemblies with both F98$_{\text{EGFR}}$ (wild type) expressing glioma cells as well as with NCI-H1975 cell lines, which are known to overexpress the double mutant T790M/L858R EGFR (Tang et al. 2008). Preliminary cytotoxicity studies were done to determine IC-50 values for the conjugates (Table 6). As can be seen, among the conjugates, the (ursolate)$_2$-MFSL conjugates showed the lowest IC-50 value for the double mutant expressing cells, while HB-VPWXE displayed the lowest IC-50 value for the wild type EGFR expressing cells. As an example, results obtained upon treatment with 3 μM concentration of the assemblies are shown in Fig. 12. As seen, the untreated F98$_{\text{EGFR}}$ (wild type) glioma cells appear healthy, and are largely spindle-shaped with fusiform nuclei, forming a twisted pattern of growth around each other (Yang et al. 2009). Upon treatment with the ursolate conjugate nanoassemblies, we did not see a significant change

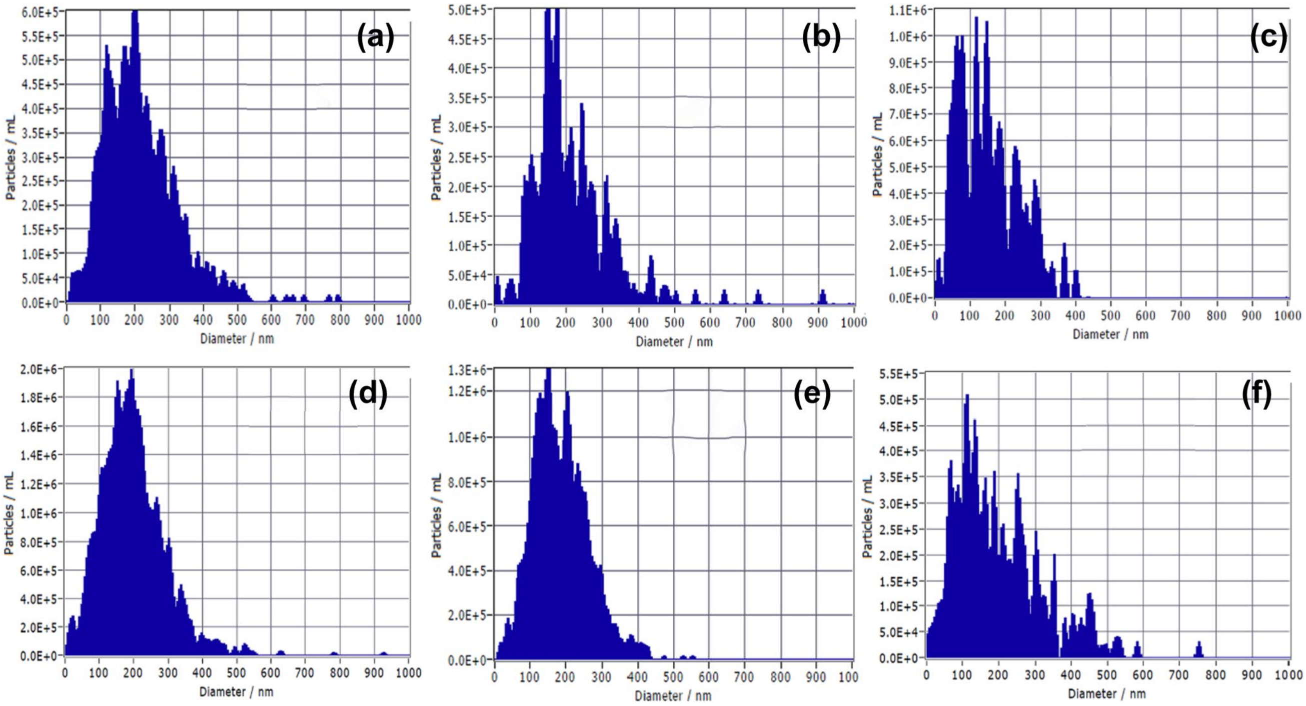

Fig. 11 NTA analysis of nanoassemblies showing size distribution. **a** HB-VPWXE; **b** oleanolate-VPWXE; **c** ursolate-VPWXE; **d** (HB)$_2$-MFSL; **e** (oleanolate)$_2$-MFSL and **f** (ursolate)$_2$-MFSL

Table 6 IC-50 values obtained for the conjugates for the NCI-H795 (T790M/L858R expressing EGFR) cells and F98 (wild type EGFR expressing cells)

Conjugate	IC-50 value (WT EGFR) (μM)	IC-50 value (T790M/L858R) (μM)
HB-VPWXE	4.7 ± 0.3	6.2 ± 1.1
Oleanolate-VPWXE	10.3 ± 2.2	8.5 ± 1.3
Ursolate-VPWXE	9.2 ± 3.1	4.6 ± 0.2
$(HB)_2$-MFSL	6.4 ± 1.4	4.9 ± 0.6
$(Oleanoate)_2$-MFSL	15.8 ± 0.7	8.2 ± 1.6
$(Ursolate)_2$-MFSL	12.7 ± 0.8	4.4 ± 0.4

in morphology. Cells appeared to cluster around each other and maintained a spindle shape morphology, although a few cells appeared to round up. Oleanolate-VPWXE, however, showed less clustering. Similar to the ursolate counterpart, a small portion of the cells appeared to be rounding up, indicative of relatively less proliferation. A similar pattern was seen for the HB-VPWXE nanoassembly treated cells. In comparison, the neat VPWXE treated cells showed long cytoskeletal extensions in some cases, while at the same time, a number of cells appeared to be rounding up, signifying declining growth of cells. This indicates that VPWXE peptide and its conjugates may be slowing down the growth of the wild type EGFR expressing cells.

In comparison, the MFSL peptide conjugates appeared to have a more significant effect in lowering the proliferation of cells and affecting cell morphology. As can be seen, in the case of the $(HB)_2$-MFSL conjugate nanoassembly treated cells, there appears to be a complete loss of spindle shape morphology of the cells, in addition to blebbing, indicating that the cell proliferation and growth was hampered by those nanoassemblies. In comparison, the $(oleanolate)_2$-MFSL and $(ursolate)_2$-MFSL conjugate nanoassemblies showed less blebbing, while few cells still appeared to maintain their actin cytoskeletal properties. These results indicate that the MSFL peptide and its conjugate nanoassemblies may be effective in targeting the cells expressing the wild type receptor expressing cells.

We then compared the effects of the nanoassemblies on the T790M/L858R expressing NCI-H1975 cells. As can be seen, the MFSL conjugates appeared to have significantly higher potency in affecting cell proliferation and morphology, with the exception of the $(oleanoate)_2$-MFSL nanoassemblies. The $(HB)_2$-MFSL nanoassembly treated cells appeared to be blebbing and fewer cells were observed overall. A similar result was seen with the HB-VPWXE treated cells where the cells showed loss of morphology, and cell ruffling along with the formation of sporadic long filopodial growth possibly due to loss of capping proteins or other factors as the cells attempt to adhere to the nanoassemblies which may trigger various changes to the mechanical and structural properties of the cells (Hein et al. 2023) and (Albuschies and Vogel 2013). The oleanolate-VPWXE nanoassemblies and the $(oleanolate)_2$-MFSL nanoassembly treated cells also showed long filopodial protrusions

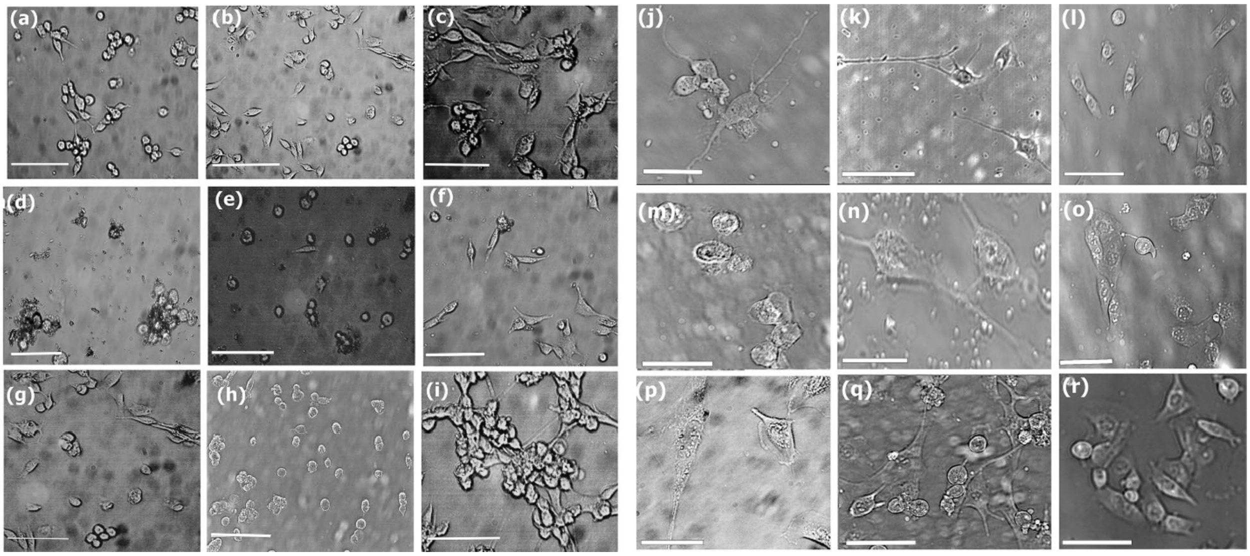

Fig. 12 Impact of growth of cells upon treatment with nanoassemblies. **a–j** F98 Wild Type EGFR expressing cells upon treatment with **a** HB-VPWXE; **b** Oleanolate-VPWXE; **c** ursolate-VPWXE; **d** $(HB)_2$-MFSL; **e** $(oleanolate)_2$-MFSL; **f** (ursolate)2-MFSL; **g** VPWXE; **h** MFSL, **i** control untreated cells. **j–r** T790M/L858R EGFR expressing NCI-H1975 cells upon treatment with **j** HB-VPWXE; **k** oleanolate-VPWXE; **l** ursolate-VPWXE; **m** $(HB)_2$-MFSL; **n** $(oleanolate)_2$-MFSL; **o** $(ursolate)_2$-MFSL; **p** VPWXE; **q** MFSL; **r** control untreated cells. Scale bar = 25 μm

extending out of the cells along with formation of actin stress fibers. The ursolate-VPWXE nanoassembly treated cells, on the other hand, did not show such extensions and a significant change in cell morphology was not seen, though a few cells appeared to round up. Thus, it appears that the MFSL peptide conjugated nanoassemblies have a higher potency in targeting the tumor cells of both cell lines, with the $(HB)_2$-MFSL nanoassemblies showing higher potency. When treated with the neat peptide, the cells were found to show membrane spreading and filopodia, and cells also appeared to be rounding up. In the case of the MFSL treated cells, we also observed a significant number of cells rounding up. This implies that the VPWXE peptide may trigger interesting mechanisms resulting filopodial outgrowths, however the MFSL peptide appears to slow down the growth to a large extent.

As an example, cell viability assays using the MTT cell proliferation assay are shown in in Fig. 13. As can be seen, the double mutant cells showed a larger reduction in proliferation. In the case of the double mutant EGFR expressing cells, $(\text{ursolate})_2$-MFSL and $(HB)_2$-MFSL showed reduction to 42% viability. However, when treated with oleanolate-VPWXE, the viability was comparatively higher, most likely because of the antioxidant effect of oleanolate moiety and this corroborates with the long filopodial growth seen for the oleanolate-peptide nanoassembly treated cells.

Nevertheless, a reduction in viability was still observed. Overall, the terpenoids conjugated with MFSL showed higher reduction in viability. This indicates that, while treatment with MFSL only showed about 28% reduction in viability, conjugating with the terpenoids further improves its cytotoxicity toward the double mutant expressing cells. For the wild type cells treated with the nanoassemblies, the lowest viability (48.3%) was seen for the HB-MFSL treated nanoassemblies, while the MFSL peptide showed a 30% reduction in viability. The $(\text{oleanolate})_2$-MFSL and oleanolate-VPWXE conjugate nanoassemblies showed similar reduction in viability (30%). Interestingly, the $(\text{ursolate})_2$-MFSL conjugate nanoassemblies induced slightly more potency in reduction in viability (39.3%). Overall, these results indicate that conjugating HB with MFSL peptide significantly reduced the viability of the wild type EGFR expressing glioma cells, however conjugating with the peptides with oleanolate did not significantly affect the viability of the cells.

As a control, we also tested the viability of non-cancer cells (fibroblasts) to examine if the conjugates are targeted toward tumor cells (Supplementary Information Fig. S6). On average, the fibroblasts continued to proliferate and demonstrated high viability (> 90% in most cases). Ursolate-VPWXE, $(HB)_2$-MFSL and VPWXE demonstrated slightly lower viability (87.2%, 88.3% and 81.1%) respectively upon treatment with the conjugates. This may be related to the fact that those conjugates that formed nanofibrillar/ nanotubular assemblies, may provide a surface that may affect cell- adhesion, though to much lower extent compared to cancer cells. However, the fibroblasts by and large continued to proliferate in the presence of the assemblies. Thus, it appears that the conjugates are more targeted toward the tumor cells. In addition to the conjugates and the peptides, we also conducted cell viability tests with the individual terpenes (Supplementary Information Fig. S7).

Viability studies were also carried out with the neat terpenoids (Supplementary Information Fig. S8). As shown, the results indicate that there was a slight reduction in viability particularly for the ursolate and oleanolate compounds (viability was found to be 76% and 75%) respectively for the treated tumor cell lines, mainly the wild type EGFR expressing cells. Almost no effect was found in fibroblasts. These results are expected as discussed earlier because the terpenes themselves have been reported to have anticancer properties. In general, conjugation with the peptide appeared to enhance tumor cell targeting and further reduce viability in most cases.

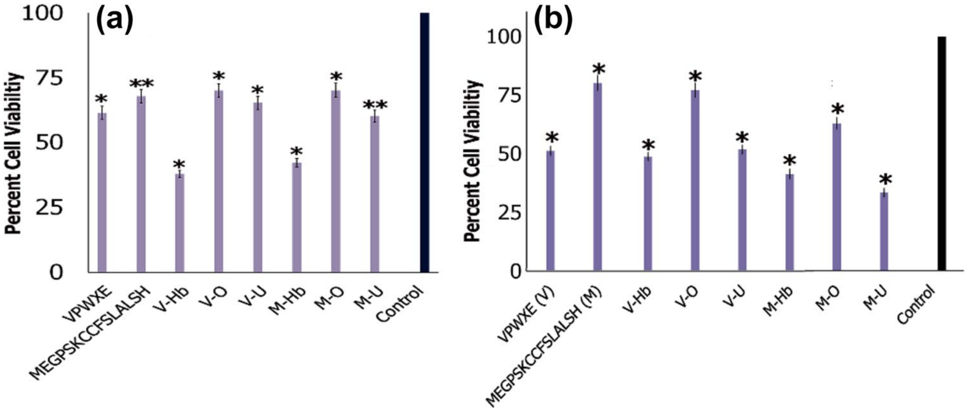

Fig. 13 Cell viability upon treatment for 24 h with various nanoassemblies at a concentration of 3 μM. **a** F98 EGFR (wild type) EGFR expressing glioma cells; **b** NCI-H1975 EGFR T790M/L858R expressing cells. *(V-Hb)* HB-VPWXE, *V–O* oleanoalate-VPWXE, *V-U* Ursolate-VPWXE, *M-HB* $(HB)_2$-MFSL, *M–O* $(\text{oleanolate})_2$-MFSL, *M-U* $(\text{ursolate})_2$-MFSL. *p value < 0.05, **p value < 0.005

Apoptosis Assay

To evaluate if the nanoassemblies induced apoptosis in the tumor cells, we carried out Annexin-FITC-propidium iodide flow cytometry assay. Results are shown in Fig. 14. In the case of the wild type EGFR expressing glioma cells, treatment with MFSL conjugates resulted in an induction of a higher amount of early apoptotic cells (between 22 and 34.3%) compared to the corresponding triterpenoid-VPWXE treated cells, which showed about 8 to 10% early apoptotic cells on average. The $(HB)_2$-MFSL nanoassemblies also displayed about 8.88% late apoptosis, indicating that it was the most potent of the conjugate nanoassemblies studied. Interestingly, however, the peptide MFSL showed the greatest effect, with 35% of cells showing late apoptosis and 29.5% of cells showing early apoptosis. Additionally, 28.1% of neat VPWXE peptide treated cells were found to show early apoptosis while 17.6% of cells displayed late apoptosis. These results corroborate with the viability studies, which also showed greater effectiveness with the MFSL conjugate nanoassemblies. In the case of T790M/L858R double mutant expressing cells, higher apoptosis was generally observed. While 28.4% of cells were found to show late apoptosis, 51.5% were found to show early apoptosis upon treatment with $(HB)_2$-MFSL nanoassemblies. On the other hand, the $(ursolate)_2$-MFSL treated cells were found to show 49% early. These results corroborate with previous studies, wherein the presence of ursolic acid has been shown to induce apoptosis in T790M/L858R expressing cells (Yang et al. 2019).

Interestingly, the HB-VPWXE conjugate also displayed higher apoptosis, (57.6% early apoptotic versus 19.5% late apoptotic). This is expected given the presence of the HB component. In previous studies, HB has been shown to induce apoptosis in tumor cells (Liu et al. 2015; Ji et al. 2002). In comparison, the oleanolate-MFSL nanoassemblies showed only 27.9% early apoptotic and about 6% late apoptotic cells. Furthermore, as in the case of the wild type, the neat MFSL peptide was found to induce early apoptosis in 20.3% of the treated cells and late apoptosis in 8.8% cells. Thus, it appears that the HB-MFSL nanoassembly is once again the most potent nanoassembly for both the wild type and the double mutant expressing cells. Additionally, the ursolate conjugates showed higher potency compared to the oleanolate conjugates, which corroborates with the fact that the ursolate component of the conjugate has been shown to have higher cytotoxicity toward tumor cells (Li et al. 2002). The corresponding results obtained for fibroblasts, which were utilized as a non-cancer cell line to ensure targeting toward cancer cells, are shown in Supplementary Information Fig. S7. As can be seen, there was very little effect of the nanoassemblies on the fibroblasts in most cases. In general, viability was seen to be greater than 85%, with the exception of $(HB)_2$-MFSL which resulted in 35% apoptotic cells which also accounts for slightly lower viability seen. These results further ascertain the fact that the nanoassemblies are more targeted toward tumor cells while

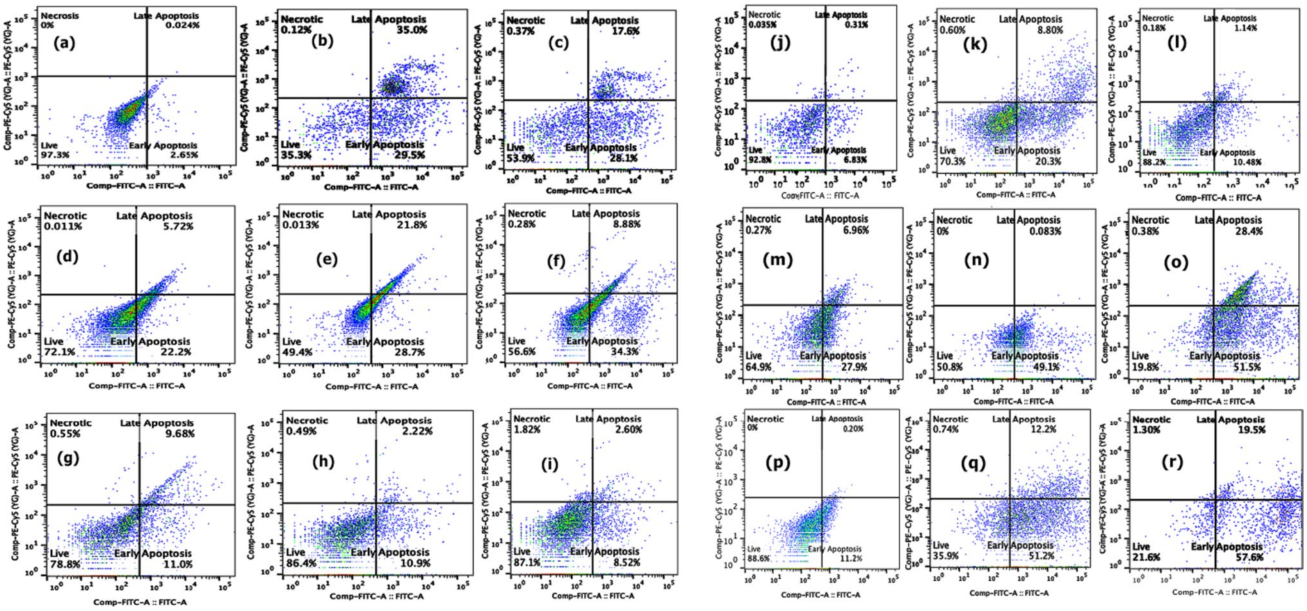

Fig. 14 Apoptosis assay using FACS analysis after 24 h of incubation with various nanoassemblies at a concentration of 3 µM. **a–i** F98 EGFR (wild type) EGFR expressing glioma cells; **a** Control untreated cells; **b** cells treated with MFSL peptide; **c** VPWXE peptide; **d** $(oleanolate)_2$-MFSL; **e** $(ursolate)_2$-MFSL; **f** $(HB)_2$-MFSL; **g** oleanoalate-VPWXE; **h** Ursolate-VPWXE; **i** HB-VPWXE. **j–r** NCI-H1975 EGFR T790M/L858R expressing lung cancer cells. **j** Control untreated cells; **k** treated with MFSL peptide; **l** VPWXE peptide; **m** $(oleanolate)_2$-MFSL; **n** $(ursolate)_2$-MFSL; **o** $(HB)_2$-MFSL; **p** oleanoalate-VPWXE; **q** Ursolate-VPWXE; **r** HB-VPWXE

the $(HB)_2$-MFSL may also show some apoptosis against non-cancer cells.

Screening of Nanoassemblies Using Glo Kinase Assay

To explore if the peptides and the conjugated peptide nanoassemblies inhibited kinase activity, we conducted the Kinase Glo assay. In this assay, the luminescence obtained correlates to the amount of ATP remaining as it works as a substrate taken up by ultra-glo luciferase reagent which then forms luciferin, resulting in luminescence. Thus, the luminescence is inversely proportional to the kinase activity. As can be seen in Fig. 14, for the wild type receptor, ursolate-VPWXE showed the lowest kinase activity, indicating highest kinase inhibition among all the conjugates and peptides. Overall, VPWXE and its conjugates displayed higher kinase inhibition compared to MFSL and its conjugates for the wild type EGFR. Among the MFSL conjugates, $(ursolate)_2$-MFSL displayed higher kinase inhibition compared to $(HB)_2$-MFSL and $(oleanolate)_2$-MFSL conjugates. These results indicate that VPWXE and its conjugates are likely binding more closely within the ATP binding pocket, resulting in an inhibitory activity. For the double mutant receptor however, the results indicated that both the MFSL and VPWXE conjugated nanoassemblies displayed significant reduction in kinase activity, with the exception of the oleanolate-VPWXE and $(oleanoate)_2$-MFSL conjugates which did not show substantial decrease in kinase activity. The reduction in activity was marginally higher for the VPWXE conjugates, while that of the $(ursolate)_2$-MFSL and the $(HB)_2$-MFSL nanoassemblies were comparable. These results indicate that the MFSL-conjugates may be more potent in binding to the kinase domain and inhibiting kinase activity of the T790M/L858R receptor, compared to that of the wild type. The VPWXE conjugates appear to bind effectively and reduce kinase activity with the exception of oleanolate-VPWXE, which showed slightly lower reduction in kinase activity. Because several of the conjugates were found to interact not only with the ATP binding pocket, but also with the allosteric residues of the kinase domain, it may be likely that some of the conjugates designed here may be potentially allosterically inhibiting the kinase activity and are not direct ATP competitive inhibitors (Fig. 15). It is also to be noted that the glo assay only takes into account the kinase reactions involving the two receptors, while at the cellular level there are several kinase and phosphatase enzymes involved and therefore those reactions may also affect ultimate results that were seen at the cellular level.

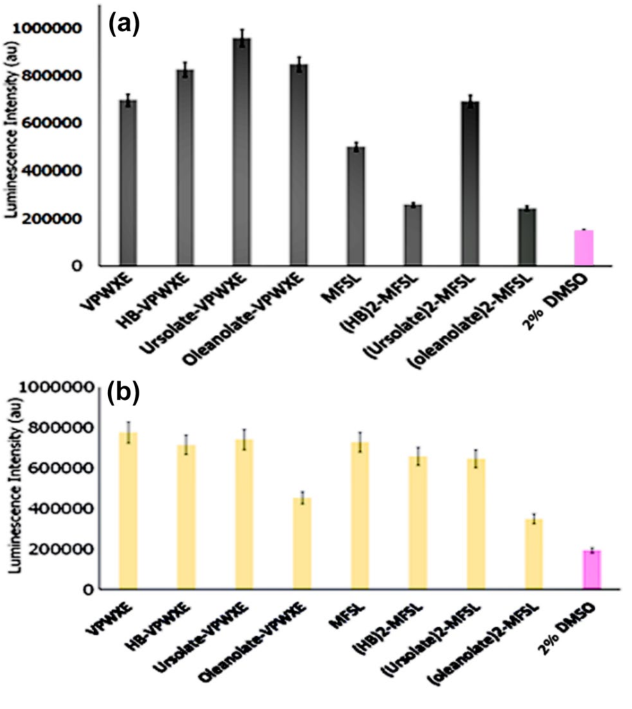

Fig. 15 A comparison of luminescence of ATP measured by Kinase glo-assay. Luminescence is inversely proportional to kinase activity. **a** VPWXE and MFSL and their conjugates upon binding with EGFR (wild type); **b** VPWXE and MFSL and their conjugates with EGFR T790M/L858R.The average values of n = 4 and standard deviation are shown

Conclusions

Peptide conjugated nanoassemblies of three pentacyclic triterpenoids, ursolic acid, hydroxybetulinic acid and oleanolic acid were designed and investigated for their ability to target EGFR expressing cell lines of the wild type and the double mutant T790M/L858R. The MEGPSKCCFSLALSH (MFSL) peptide was created to target EGFR by mutating the MEGPSKCCYSLALSH peptide sequence at position nine, while the VPWXE peptide belongs to a segment of the peptide motif known to bind to tumor cells. Upon self-assembly, the conjugates formed either nanofibers, nanospheres or multilayered supramolecular structures. Docking studies revealed that the conjugates formed hydrogen bonds with several residues within the ATP binding pocket. The $(oleanolate)_2$-MFSL and $(ursolate)_2$-MFSL conjugates interacted with key residues such as LYS 721 and ARG 817, while the $(hydroxybetulinate)_2$-MSFL conjugate interacted with the DFG motif residue ASP 831, as did the neat peptide. The VPWXE peptide and its conjugates displayed interactions within the hinge region as well as with the A-loop residues. For the EGFR T790M/L858R, the ursolate-VPWXE conjugate formed hydrogen bonds with critical residues such as MET 793, CYS 797, ARG 841, LYS 745 and TRP 880, while the other conjugates also interacted with allosteric regions deeper into the C-terminal region of the receptor. Laboratory studies with cells expressing the wild type and the double mutant receptor revealed that higher apoptosis was induced by MFSL conjugates in cells expressing the double mutant receptor. Additionally, the MFSL conjugates showed a marked decrease in kinase activity, particularly for the double mutant receptor, while VPWXE conjugates had showed greater reduction in kinase activity of the wild type receptor. Overall, these results indicate that both peptides can effectively bind to the wild type and the T790M/L858R receptor. Additionally, the peptide conjugated ursolate and HB terpenes may further improve their effectiveness and targeting ability of the terpenoids and thus may be developed for further studies for developing therapeutics.

Supplementary Information The online version contains supplementary material available at https://doi.org/10.1007/s10989-023-10583-6.

Acknowledgements All authors thank the Advanced Research Computing, Education Technologies and Research Computing department at Fordham University, a division of the Office of Information Technology for providing their assistance and access to research computing resources that have contributed to the results reported here. IB also thanks the Keck Biotechnology Laboratory for help with NTA experiments.

Author Contributions MR and BG—In silico modeling, interpretation of data, data curation, in vitro studies, data analysis and writing parts of the manuscript; HH: In vitro studies including viability and FACS assays and writing and editing parts of the manuscript. IB: Conceptualization, supervision, experimental design, data analysis, editing and writing the final version of the manuscript.

Funding IB thanks NSF-MRI grant # 1626378 and NSF-MRI grant # 2117625 for the acquisition of the AFM and the FACS instruments respectively. IB also thanks the research office at Fordham University for financial support. BG and HH thank the Henry Luce Foundation for the Clare Boothe Luce Scholarship for financial support of this work. IB thanks the Fordham University research office for financial support.

Data Availability Associated data are included in the supplementary information. The manuscript will be shared on faculty website.

Code Availability NA.

Declarations

Competing interests The authors declare no conflict of interest.

Ethics Approval and Consent to Participate N/A.

References

Agarwal SM, Nandekar P, Saini R (2022) Computational identification of natural product inhibitors against EGFR double mutant (T790M/L858R) by integrating ADMET, Machine Learning, molecular docking and a dynamics approach. RSC Adv 12(26):16779–16789. https://doi.org/10.1039/d2ra00373b

Ahmadpour S, Hosseinimehr SJ (2019) Recent developments in peptide-based SPECT radiopharmaceuticals for breast tumor targeting. Life Sci 239:116870. https://doi.org/10.1016/j.lfs.2019.116870

Ahmed S, Kaur K (2017) Design, synthesis and validation of an in vitro platform peptide-whole cell screening assay using MTT reagent. J Taibah Univ Sci 11(3):487–496. https://doi.org/10.1016/j.jtusci.2016.10.001

Albuschies J, Vogel V (2013) The role of filopodia in the recognition of nanotopographies. Sci Rep 3:1658. https://doi.org/10.1038/srep01658

Askoxylakis V, Mier W, Zitzmann S, Ehemann V, Zhang J, Krämer S, Beck C, Schwab M, Eisenhut M, Haberkorn U (2006) Characterization and development of a peptide (p160) with affinity for neuroblastoma cells. J Nucl Med 47(6):981–988

Azuaje F (2017) Computational models for predicting drug responses in cancer research. Brief Bioinform 18(5):820–829. https://doi.org/10.1093/bib/bbw065

Bag BG, Paul K (2012) Vesicular and fibrillar gels by self-assembly of nanosized oleanolic acid. Asian J Org Chem 1:150–154. https://doi.org/10.1002/ajoc.201200032

Bag BG, Das S, Hasan SN, Barai AC (2017) Nanoarchitectures by hierarchical self-assembly of ursolic acid: entrapment and release of fluorophores including anticancer drug doxorubicin. RSC Adv 7(29):18136–18143. https://doi.org/10.1039/C7RA02123B

Banks JL, Beard HS, Cao Y, Cho AE, Damm W, Farid R, Felts AK, Halgren TA, Mainz DT, Maple JR, Murphy R, Philipp DM, Repasky MP, Zhang LY, Berne BJ, Friesner RA, Gallicchio E, Levy RM (2005) Integrated Modeling Program, Applied Chemical Theory (IMPACT). J Comput Chem 26(16):1752–1780. https://doi.org/10.1002/jcc.20292

Barker AJ, Gibson KH, Grundy W, Godfrey AA, Barlow JJ, Healy MP, Woodburn JR, Ashton SE, Curry BJ, Scarlett L, Henthorn L, Richards L (2001) Studies leading to the identification of ZD1839 (Iressa™): an orally active, selective epidermal growth factor receptor tyrosine kinase inhibitor targeted to the treatment of cancer. Bioorg Med Chem Lett 11(14):1911–1914. https://doi.org/10.1016/s0960-894x(01)00344-4

Bell RA, Storey KB (2014) Novel detection method for chemiluminescence derived from the Kinase-Glo luminescent kinase assay platform: advantages over traditional microplate luminometers. MethodsX 1:96–101. https://doi.org/10.1016/j.mex.2014.07.003

Bergdorf M, Baxter S, Rendleman CA, Shae DE (2016) Desmond/GPU performance as of November 2016. D.E. Shaw Research Technical Report DESRES/T-2019-01. https://www.deshawresearch.com/publications/Desmond-GPU%20Performance%20as%20of%20November%202016.pdf. Accessed 27 July 2023

Beyett TS, To C, Heppner DE, Rana JK, Schmoker AM, Jang J, Clercq D, Gomez G, Scott D, Gray NS, Janne P, Eck MJ (2022) Molecular basis for cooperative binding and synergy of ATP-site and allosteric EGFR inhibitors. Nat Commun 13(1):2530. https://doi.org/10.1038/s41467-022-30258-y

Bose R, Zhang X (2009) ErbB kinase domain: structural perspectives into kinase activation and inhibition. Exp Cell Res 315(4):649–658. https://doi.org/10.1016/j.yexcr.2008.07.031

Bowers KJ, Chow E, Xu H, Dror RO, Eastwood MP, Gregersen BA, Klepeis JL, Kolossvary I, Moraes MA, Sacerdoti FD, Salmon JK, Shan Y, Shaw DE (2006) Molecular Dynamics—Scalable algorithms for molecular dynamics simulations on commodity clusters. In: Proc ACM/IEEE Conf SC06 84-es. https://doi.org/10.1145/1188455.1188544

Carvalho I, Milanezi F, Martins A, Reis RM, Schmitt F (2005) Overexpression of platelet-derived growth factor receptor alpha in breast cancer is associated with tumour progression. Breast Cancer Res 7(5):R788–R795. https://doi.org/10.1186/bcr1304

Cataldo VD, Gibbons DL, Pérez-Soler R, Quintás-Cardama A (2011) Treatment of non-small cell lung cancer with erlotinib or gefitinib. N Engl J Med 364(10):947–955. https://doi.org/10.1056/NEJMct0807960

Chadalapaka G, Jutooru I, Burghardt R, Safe S (2010) Drugs that target specificity proteins downregulate epidermal growth factor receptors in bladder cancer cells. Mol Cancer Res 8(5):739–750. https://doi.org/10.1158/1541-7786.MCR-09-0493

Chen S, Zhao X, Chen J, Chen J, Kuznetsova L, Wong SS, Ojima I (2010) Mechanism-based tumor-targeting drug delivery system Validation of efficient vitamin receptor-mediated endocytosis and drug release. Bioconj. Chem 21(5):979–987. https://doi.org/10.1021/bc9005656

Cheng Z, Li M, Dey R, Chen Y (2021) Nanomaterials for cancer therapy: current progress and perspectives. J Hematol Oncol 14(1):85. https://doi.org/10.1186/s13045-021-01096-0

Costa SA, Mozhdehi D, Dzuricky MJ, Isaacs FJ, Brustad EM, Chilkoti A (2019) Active targeting of cancer cells by nanobody decorated polypeptide micelle with bio-orthogonally conjugated drug. Nano Lett 19(1):247–254. https://doi.org/10.1021/acs.nanolett.8b03837

Dasmahapatra U, Kumar CK, Das S, Subramanian PT, Murali P, Isaac AE, Ramanathan K, Mm B, Chanda K (2022) In-silico molecular modelling, MM/GBSA binding free energy and molecular dynamics simulation study of novel pyrido fused imidazo[4,5-c]quinolines as potential anti-tumor agents. Front Chem 10:991369. https://doi.org/10.3389/fchem.2022.991369

Debala DT, Muzazu SGY, Heraro KD, Ndalama MT, Mesele BW, Haile DC, Kitui SK, Mayazewal T (2021) New approaches and procedures for cancer treatment: current perspectives. Sage Open Med 9:20503121211034370. https://doi.org/10.1177/20503121211034366

Du Z, Lovly CM (2018) Mechanisms of receptor tyrosine kinase activation in cancer. Mol Cancer. https://doi.org/10.1186/s12943-018-0782-4

Durrant JD, McCammon JA (2011) Molecular dynamics simulations and drug discovery. BMC Biol 9:71. https://doi.org/10.1186/1741-7007-9-71

Emami L, Khabnadideh S, Faghih Z, Farahvasi F, Zonobi F, Gheshlaghi SZ, Daili S, Ebrahimi A, Faghih Z (2022) Synthesis, biological evaluation, and computational studies of some novel quinazoline derivatives as anticancer agents. BMC Chem 16(1):100. https://doi.org/10.1186/s13065-022-00893-z

Ferdausi N, Islam S, Rimti FH, Quayum ST, Arshad EM, Ibnat A, Islam T, Arefin A, Ema TI, Biswas P, Dey D, Al Azad S (2022) Point-specific interactions of isovitexin with the neighboring amino acid residues of the hACE2 receptor as a targeted therapeutic agent in suppressing the SARS-CoV-2 influx mechanism. J Adv Vet Anim Res 9(2):230–240. https://doi.org/10.5455/javar.2022.i588

Filipe V, Hawe A, Jiskoot W (2010) Critical evaluation of nanoparticle tracking analysis (NTA) by nanosight for the measurement by NanoSight for the measurement of nanoparticles and protein aggregates. Pharm Res 27(5):796–810. https://doi.org/10.1007/s11095-010-0073-2

Fischer M (2010) Amine coupling through EDC/NHS: a practical approach. Methods Mol Biol 627:55–73. https://doi.org/10.1007/978-1-60761-670-2_3

Forouzesh N, Mishra N (2021) An effective MM/GBSA protocol for absolute binding free energy calculations: a case study on SARS-CoV-2 spike protein and the human ACE2 receptor. Molecules 26(8):2383. https://doi.org/10.3390/molecules26082383

Fry DW, Bridges AJ, Denny WA, Doherty A, Greis KD et al (1998) Specific, irreversible inactivation of the epidermal growth factor receptor and erbB2, by a new class of tyrosine kinase inhibitor. Proc Natl Acad Sci USA 95(20):12022–12027. https://doi.org/10.1073/pnas.95.20.12022

Gajiwala KS, Feng J, Ferre R, Ryan K, Brodsky O, Weinrich S, Kath JC, Stewart A (2013) Insights into the aberrant activity of mutant EGFR kinase domain and drug recognition. Structure 21(2):209–219. https://doi.org/10.1016/j.str.2012.11.014

Gao H, Wang Y, Chen C, Chen J, Wei Y, Cao S, Jiang X (2014) Incorporation of lapatinib into core-shell nanoparticles improves both the solubility and anti-glioma effects of the drug. Int J Pharm 461(1–2):478–488. https://doi.org/10.1016/j.ijpharm.2013.12.016

Genheden S, Ryde U (2015) The MM/PBSA and MM/GBSA methods to estimate ligand-binding affinities. Expert Opin Drug Discov 10(5):449–461. https://doi.org/10.1517/17460441.2015.1032936

Ghandehari F, Behbahani M, Pourazar A, Noormohammadi Z (2015) In silico and in vitro studies of cytotoxic activity of different peptides derived from vesicular stomatitis virus G protein. Iran J Basic Med Sci 18(1):47–52. https://doi.org/10.5812/jkums.69544

Ghasemi M, Turnbull T, Sebastian S, Kempson I (2021) The MTT assay: utility, limitations, pitfalls and interpretation in bulk and single-cell analysis. Int J Mol Sci 22(23):12827. https://doi.org/10.3390/ijms222312827

Ghosh S, Bishayee K, Khuda-Bukhsh AR (2014) Oleanolic acid isolated from ethanolic extract of Phytolacca decandra induces apoptosis in A375 skin melanoma cells: drug-DNA interaction and signaling cascade. J Integr Med 12(2):102–114. https://doi.org/10.1016/S2095-4964(14)60015-7

Gu G, Hu Q, Feng X, Gao X, Menglin J, Kang T, Jiang D, Song Q, Chen H, Chen J (2014) PEG-PLA nanoparticles modified with APTEDB peptide for enhanced anti-angiogenic and anti-glioma therapy. Biomaterials 35(28):8215–8226. https://doi.org/10.1016/j.biomaterials.2014.06.022

Gurrapu N, Praveen Kumar E, Kolluri PK, Putta S, Sivan SK, Subhashini NJP (2020) Synthesis, biological evaluation and molecular docking studies of novel 1,2,3-triazole tethered chalcone hybrids as potential anticancer agents. J Mol Struc 1217:128356. https://doi.org/10.1016/j.molstruc.2020.128356

Hein JI, Scholz J, Köber S, Kaufmann T, Faix J (2023) Unleashed actin assembly in capping protein deficient B16–F1 cells enables identification of multiple factors contributing to filopodium formation. Cells 12(6):890. https://doi.org/10.3390/cells12060890

Honegger AM, Dull TJ, Felder S, VanObberghen E, Bellot F, Szapary D, Schmidt A, Schlessinger J (1987) Point mutation at the ATP binding site of EGF receptor abolishes protein-tyrosine kinase activity and alters cellular routing. Cell 51:199–209. https://doi.org/10.1016/0092-8674(87)90147-4

Jagtap JM, Parchur AK, Sharma G (2020) Smart nanomaterials for tumor targeted hyperthermia. In: Ahmad N, Gopinath P (eds) Intelligent nanomaterials for drug delivery applications. Chp. 3, pp 43–59

Ji ZN, Ye WC, Liu GG, Hsiao WL (2002) 23-Hydroxybetulinic acid-mediated apoptosis is accompanied by decreases in bcl-2 expression and telomerase activity in HL-60 Cells. Life Sci 72(1):1–9. https://doi.org/10.1016/s0024-3205(02)02176-8

Juul-Madsen K, Troldborg A, Wittenborn T, Axelsen M, Zhao H, Klausen L, Luecke S, Paludan S, Stengaard-Pedersen K, Dong M, Moller H, Thiel S, Jensen H, Schuck P, Sutherland D, Degn S, Vorup-Jensen T (2021) Characterization of DNA-protein complexes by nanoparticle tracking analysis and their association with systemic lupus. PNAS 118(30):e2106647118. https://doi.org/10.1073/pnas.2106647118

Kovacs E, Zorn JA, Huang Y, Barros T, Kuriyan J (2015) A structural perspective on the regulation of the EGF receptor. Annu Rev Biochem 84:739–764. https://doi.org/10.1146/annurev-biochem-060614-034402

Kumar A, Petri ET, Halmos B, Boggon TJ (2008) Structure and clinical relevance of the epidermal growth factor receptor. J Clin Oncol 26(10):1742–1751. https://doi.org/10.1200/JCO.2007.12.1178

Kumar BK, Faheem SKVGC, Ojha R, Prajapati VK, Pai A, Murugesan S (2022) Pharmacophore based virtual screening, molecular docking, molecular dynamics and MM-GBSA approach for identification of prospective SARS-CoV-2 inhibitor from natural product databases. J Biomol Struct Dyn 40(3):1363–1386. https://doi.org/10.1080/07391102.2020.1824814

Kutova OM, Guryev EL, Sokolova EA, Alzeibak R, Balalaeva IV (2019) Targeted delivery to tumors: multidirectional strategies to improve treatment efficiency. Cancers 11(1):68. https://doi.org/10.3390/cancers11010068

Lee HJ, Seo AN, Kim EJ, Jang MH, Kim YJ, Kim JH, Kim SW, Ryu HS, Park IA, Im SA, Gong G, Jung KH, Kim HJ, Park SY (2015) Prognostic and predictive values of EGFR overexpression and EGFR copy number alteration in HER2-positive breast cancer. Br J Cancer 112(1):103–111. https://doi.org/10.1038/bjc.2014.556

Lelais G, Epple R, Marsilje TH, Long YO, McNeill M, Chen B, Lu W, Anumolu J, Badiger S, Bursulaya B, DiDonato M, Fong R, Juarez J, Li J, Manuia M, Mason DE, Gordon P, Groessl T, Johnson K, Jia Y, Kasibhatla S, Li C, Isbell J, Spraggon G, Bender S, Michellys PY (2016) Discovery of (R, E)-N-(7-Chloro-1-(1-[4-(dimethylamino)but-2-enoyl]azepan-3-yl)-1H-benzo[d]imidazol-2-yl)-2-methylisonicotinamide (EGF816), a novel, potent, and WT sparing covalent inhibitor of oncogenic (L858R, ex19del) and resistant (T790M) EGFR mutants for the treatment of EGFR mutant non-small-cell lung cancers. J Med Chem 59(14):6671–6689. https://doi.org/10.1021/acs.jmedchem.5b01985

Li J, Guo WJ, Yang QY (2002) Effects of ursolic acid and oleanolic acid on human colon carcinoma cell line HCT15. World J Gastroenterol 8(3):493–495. https://doi.org/10.3748/wjg.v8.i3.493

Li S, Huang S, Peng SB (2005) Overexpression of G protein-coupled receptors in cancer cells: involvement in tumor progression. Int J Oncol 27(5):1329–1339. https://doi.org/10.3892/ijo.27.5.1329

Liao SM, Du QS, Meng JZ, Pang ZW, Huang RB (2013) The multiple roles of histidine in protein interactions. Chem Cent J 7(1):44. https://doi.org/10.1186/1752-153X-7-44

Limonta P, Montagnani Marelli M, Mai S, Motta M, Martini L, Moretti RM (2012) GnRH receptors in cancer: from cell biology to novel targeted therapeutic strategies. Endocr Rev 33(5):784–811. https://doi.org/10.1210/er.2012-1014

Liu M, Zhao X, Xiao L, Liu G, Liu H, Wang X, Feng X, Lin X (2015) Cytotoxicity of the compounds isolated from *Pulsatilla chinensis* saponins and apoptosis induced by 23-hydroxybetulinic acid. Pharm Biol 53(1):1–9. https://doi.org/10.3109/13880209.2014.907323

Lowder MA, Doerner AE, Schepartz A (2015) Structural differences between wild type and double mutant EGFR modulated by third-generation kinase inhibitors. J Am Chem Soc 137(20):6456–6459. https://doi.org/10.1021/jacs.5b02326

Lu L, Zhang H, Liu J, Liu Y, Wang Y, Xu S, Zhu Z, Xu J (2019) Synthesis, biological evaluation and mechanism studies of C-23 modified 23-hydroxybetulinic acid derivatives as anticancer agents. Eur J Med Chem 182:111659. https://doi.org/10.1016/j.ejmech.2019.111659

Luo Z, Akerman B, Zhang S, Norden B (2010) Structures of self-assembled amphiphilic peptide-heterodimers: effects of concentration, pH, temperature and ionic strength. Soft Matter 6:2260–2270. https://doi.org/10.1039/B926962B

Maennling AE, Tur MK, Niebert M, Klockenbring T, Zeppernick F, Gattenlöhner S, Meinhold-Heerlein I, Hussain AF (2019) Molecular targeting therapy against EGFR family in breast cancer: Progress and future potentials. Cancers 11(12):1826. https://doi.org/10.3390/cancers11121826

Martin-Fernandez ML, Clarke DT, Roberts SK, Zanetti-Domingues LC, Gervasio FL (2019) Structure and dynamics of the EGF receptor as revealed by experiments and simulations and its relevance to non-small cell lung cancer. Cells 8(4):316. https://doi.org/10.3390/cells8040316

Masuda H, Zhang D, Bartholomeusz C, Doihara H, Hortobagyi GN, Ueno NT (2012) Role of epidermal growth factor receptor in breast cancer. Breast Cancer Res Treat 136(2):331–345. https://doi.org/10.1007/s10549-012-2289-9

McKinnon KM (2018) Flow cytometry: an overview. Curr Protoc Immunol 120:5.1.1-5.1.11. https://doi.org/10.1002/cpim.40

Mehmankhah M, Ramachandran S, Alam MA (2014) Predicting probable ligands to inhibit HER2-EGFR in gastric cancer. IOSR J Pharm Biol Sci 9(3):37–49. https://doi.org/10.9790/3008-09363749

Minashi K, Yamada T, Hosaka H, Amagai K, Shimizu Y, Kiyozaki H, Sato M, Soeda A, Endo S, Ishida H, Kamoshida T, Sakai Y, Shitara K (2021) Cancer related FGFR2 overexpression and gene amplification in Japanese patients with gastric cancer. Jpn J Clin Oncol 51(10):1523–1533. https://doi.org/10.1093/jjco/hyab104

Minnelli C, Laudadio E, Mobbili G, Galeazzi R (2020) Conformational insight on WT- and mutated EGFR receptor activation and inhibition by epigallocatechin-3-gallate: over a rational basis for the design of selective non-small cell lung cancer anticancer agents. Int J Mol Sci 21(5):1721. https://doi.org/10.3390/ijms21051721

Mirza Z, Schulten HJ, Farsi H, Al-Maghrabi JA, Gari MA, Chaudhary AG, Abuzenadah AM, Al-Qahtani MH, Karim S (2015) Molecular interaction of a kinase inhibitor Midostaurin with anticancer drug targets, S100A8 and EGFR: transcriptional profiling and molecular docking study for kidney cancer therapeutics. PLoS ONE 10(3):e0119765. https://doi.org/10.1371/journal.pone.0119765

Morency LP, Gaudreault F, Najmanovich R (2018) Applications of the NRGsuite and the molecular docking software FlexAID in computational drug discovery and design. Methods Mol Biol 1762:367–388. https://doi.org/10.1007/978-1-4939-7756-7_18

Mukund V, Saddala MS, Farran B, Mannavarapu M, Alam A, Nagaraju GP (2019) Molecular docking studies of angiogenesis target protein HIF-1α and genistein in breast cancer. Gene 701:169–172. https://doi.org/10.1016/j.gene.2019.03.062

Mulyadi M (2011) Cytotoxicity test pentacyclic triterpenes of Eupatorium inulifolium HBK on myeloma cells and their docking study. Indonesian J Pharm 22(3):182–190

Nguyen KS, Kobayashi S, Costa DB (2009) Acquired resistance to epidermal growth factor receptor tyrosine kinase inhibitors in non-small cell lung cancers dependent on the epidermal growth factor receptor pathway. Clin Lung Cancer 10(4):281–289. https://doi.org/10.3816/CLC.2009.n.039

Ovesná Z, Kozics K, Slamenová D (2006) Protective effects of ursolic acid and oleanolic acid in leukemic cells. Mutat Res 600(1–2):131–137. https://doi.org/10.1016/j.mrfmmm.2006.03.008

Palanivel S, Yli-Harja O, Kandhavelu M (2022) Molecular interaction study of novel indoline derivatives of EGFR-kinase domain using multiple computational analysis. J Biomol Struc Dyn 40(16):7545–7554. https://doi.org/10.1080/07391102.2021.1900917

Peng YH, Shiao HY, Tu CH, Liu PM, Hsu JT, Amancha PK, Wu JS, Coumar MS, Chen CH, Wang SY, Lin WH, Sun HY, Chao YS, Lyu PC, Hsieh HP, Wu SY (2013) Protein kinase inhibitor design by targeting the Asp-Phe-Gly (DFG) motif: the role of the DFG motif in the design of epidermal growth factor receptor inhibitors. J Med Chem 56(10):3889–3903. https://doi.org/10.1021/jm400072p

Purba ER, Saita EI, Maruyama IN (2017) Activation of the EGF receptor by ligand binding and oncogenic mutations: the “Rotation Model.” Cells 6(2):13. https://doi.org/10.3390/cells6020013

Ramirez D, Caballero J (2018) Is it reliable to take the molecular docking top scoring position as the best solution without considering available structural data. Molecules 23(5):1038. https://doi.org/10.3390/molecules23051038

Rashid H, Ahmad N, Abdalla M, Khan K, Utera Martines MA, Shabana S (2022) Molecular docking and dynamic simulations of Cefixime, Etoposide and Nebrodenside A against pathogenic proteins of SARS-CoV-2. J Mol Struct 1247:131296. https://doi.org/10.1016/j.molstruc.2021.131296

Rieger AM, Nelson KL, Konowalchuk JD, Barreda DR (2011) Modified annexin V/propidium iodide apoptosis assay for accurate assessment of cell death. J Vis Exp 50:2597. https://doi.org/10.3791/2597

Rimawi MF, Shetty PB, Weiss HL, Schiff R, Osborne CK, Chamness GC, Elledge RM (2010) Epidermal growth factor receptor expression in breast cancer association with biologic phenotype and clinical outcomes. Cancer 116(5):1234–1242. https://doi.org/10.1002/cncr.24816

Roskoski RJ (2016) Classification of small molecule protein kinase inhibitors based upon the structures of their drug-enzyme complexes. Pharmacol Res 103:26–48. https://doi.org/10.1016/j.phrs.2015.10.021

Salentin S, Haupt VJ, Daminelli S, Schroeder M (2014) Polypharmacology rescored: protein-ligand interaction profiles for remote binding site similarity assessment. Prog Biophys Mol Biol 116(2–3):174–186. https://doi.org/10.1016/j.pbiomolbio.2014.05.006

Shan JZ, Xuan YY, Zheng S, Dong Q, Zhang SZ (2009) Ursolic acid inhibits proliferation and induces apoptosis of HT-29 colon cancer cells by inhibiting the EGFR/MAPK pathway. J Zhejiang Univ Sci B 10(9):668–674. https://doi.org/10.1631/jzus.B0920149

Sheikh IA, Hassan HM (2016) In silico identification of novel erlotinib analogues against epidermal growth factor receptor. Anticancer Res 36(11):6125–6132. https://doi.org/10.21873/anticanres.11203

Shibuya M (2011) Vascular endothelial growth factor (VEGF) and its receptor (VEGFR) signaling in angiogenesis. Genes Cancer 2(12):1097–1105. https://doi.org/10.1177/1947601911423031

Suenaga A, Okimoto N, Hirano Y, Fukui K (2012) An efficient computational method for calculating ligand binding affinities. PLoS ONE 7(8):e42846. https://doi.org/10.1371/journal.pone.0042846

Tamirat MZ, Koivu M, Elenius K, Johnson MS (2019) Structural characterization of EGFR exon 19 deletion mutation using molecular dynamics simulation. PLoS ONE 14(9):e0222814. https://doi.org/10.1371/journal.pone.0222814

Tang Z, Du R, Jiang S, Wu C, Barkauskas DS et al (2008) Dual MET-EGFR combinatorial inhibition against T790M-EGFR-mediated erlotinib-resistant lung cancer. Br J Cancer 99(6):911–922. https://doi.org/10.1038/sj.bjc.6604559

Tang ZY, Li Y, Tang YT, Ma XD, Tang ZY (2022) Anticancer activity of oleanolic acid and its derivatives: recent advances in evidence, target profiling and mechanisms of action. Biomed Pharmacother 145:112397. https://doi.org/10.1016/j.biopha.2021.112397

Tarasov SG, Gaponenko V, Howard OM, Chen Y, Oppenheim JJ, Dyba MA, Subramaniam S, Lee Y, Michejda C, Tarasova NI (2011) Structural plasticity of a transmembrane peptide allows self-assembly into biologically active nanoparticles. Proc Natl Acad Sci USA 108(24):9798–9803. https://doi.org/10.1073/pnas.1014598108

Trott O, Olson AJ (2012) AutoDock Vina: improving the speed and accuracy of docking with a new scoring function, efficient optimization and multithreading. J Comput Chem 31(2):455–461. https://doi.org/10.1002/jcc.21334

Vijayakumar S, Lakshmi PTV (2015) ACPP: a web server for prediction and design of anti-cancer peptides. Int J Pept Res Ther 21(1):99–106. https://doi.org/10.1007/s10989-014-9435-7

Volante M, Rosas R, Allìa E, Granata R, Baragli A, Muccioli G, Papotti M (2008) Somatostatin, cortistatin and their receptors in tumors. Mol Cell Endocrinol 286(1–2):219–229. https://doi.org/10.1016/j.mce.2007.12.002

Wang YK, Gao CF, Yun T, Chen Z, Zhang XW, Lv XX, Meng NL, Zhao WZ (2011) Assessment of ERBB2 and EGFR gene amplification and protein expression in gastric carcinoma by immunohistochemistry and fluorescence in situ hybridization. Mol Cytogenet 4(1):14. https://doi.org/10.1186/1755-8166-4-14

Worm DJ, Els-Heindl S, Beck-Sickinger AG (2020) Targeting of peptide-binding receptors on cancer cells with peptide-drug conjugates. Pept Sci 112(3):24171. https://doi.org/10.1002/pep2.24171

Yang W, Barth RF, Wu G, Huo T, Tjarks W, Ciesielski M, Fenstermaker RA, Ross BD, Wikstrand CJ, Riley KJ, Binns PJ (2009) Convection enhanced delivery of boronated EGF as a molecular targeting agent for neutron capture therapy of brain tumors. J Neurooncol 95(3):355–365. https://doi.org/10.1007/s11060-009-9945-x

Yang K, Chen Y, Zhou J, Ma L, Shan Y, Cheng X, Wang Y, Zhang Z, Ji X, Chen L, Dai H, Zhu B, Li C, Tao Z, Hu X, Yin W (2019) Ursolic acid promotes apoptosis and mediates transcriptional suppression of CT45A2 gene expression in non-small–cell lung carcinoma harboring EGFR T790M mutations. Br J Pharmacol 176(24):4609–4624. https://doi.org/10.1111/bph.14793

Yeruva L, Pierre KJ, Elegbede A, Wang RC, Carper SW (2007) Perillyl alcohol and perillic acid induced cell cycle arrest and apoptosis in non small cell lung cancer cells. Cancer Lett 257(2):216–226. https://doi.org/10.1016/j.canlet.2007.07.020

Yin R, Li T, Tian JX, Xi P, Liu RH (2017) Ursolic acid, a potential anticancer compound for breast cancer therapy. Crit Rev Food Sci Nutr 58(4):568–574. https://doi.org/10.1080/10408398.2016.1203755

Yu J, Zhou Y, Tanaka I, Yao M (2010) Roll: a new algorithm for the detection of protein pockets and cavities with a rolling probe sphere. Bioinformatics 26(1):46–52. https://doi.org/10.1093/bioinformatics/btp599

Yu HA, Arcila ME, Hellmann MD, Kris MG, Ladanyi M, Riely GJ (2014) Poor response to erlotinib in patients with tumors containing baseline EGFR T790M mutations found by routine clinical molecular testing. Ann Oncol 25(2):423–428. https://doi.org/10.1093/annonc/mdt573

Zhang X, Gureasko J, Shen K, Cole PA, Kuriyan J (2006) An allosteric mechanism for activation of the kinase domain of epidermal growth factor receptor. Cell 125(6):1137–1149. https://doi.org/10.1016/j.cell.2006.05.013

Zhang XY, Zhang YK, Wang YJ, Gupta P, Zeng L, Xu M, Wang XQ, Yang DH, Chen ZS (2016) Osimertinib (AZD9291), a mutant selective EGFR inhibitor, reverses ABCB1-mediated drug resistance in cancer cells. Molecules 21(9):1236. https://doi.org/10.3390/molecules21091236

Zhang X, Sanchez-Perez H, Lightsone FC (2017) A comprehensive docking and MM/GBSA rescoring study of ligand recognition upon binding antithrombin. Curr Top Med Chem 17(14):1631–1639

Zhao P, Yao MY, Zhu SJ, Chen JY, Yun CH (2018) Crystal structure of EGFR T790M/C797S/V948R in complex with EAI045. Biochem Biophys Res Commun 502(3):332–337. https://doi.org/10.1016/j.bbrc.2018.05.154

Zhao Z, Xie L, Bourne PE (2020) Structural insights into characterizing binding sites in EGFR kinase mutants. J Chem Inf Model 59(1):453–462. https://doi.org/10.1021/acs.jcim.8b00458

Zhu SJ, Zhao P, Yang J, Ma R, Yan XE, Yang SY, Yang JW, Yun CH (2018) Structural insights into drug development strategy targeting EGFR T90M/C797S. Oncotarget 9(17):13652–13665. https://doi.org/10.18632/oncotarget.24113